Nonequilibrium Flow Simulations Using Unified Gas-Kinetic Wave-Particle Method

Wenpei Long,* Yufeng Wei,† and Kun Xu‡
The Hong Kong University of Science and Technology, Hong Kong Special Administrative Region, People's Republic of China

https://doi.org/10.2514/1.J063641

Nonequilibrium flows are commonly encountered in aerospace engineering applications such as spacecraft reentry, rocket launch, and satellite attitude control. Numerical simulations help greatly in the understanding of nonequilibrium flow, multiscale effects, and the dynamics in these applications. Coupling particle transport and collision within the gas evolution process, the unified gas-kinetic wave-particle (UGKWP) method has been developed for multiscale flow simulation, offering a strategy that strikes a balance between accuracy and efficiency. In the present study, the UGKWP method simulates challenging flow problems with large Knudsen number variations, including supersonic flow around a sphere, hypersonic flow around a space vehicle, nozzle plume into vacuum, and side-jet impingement on the hypersonic flow. The UGKWP accurately captures complex flow structures and has been verified through experimental data or direct simulation Monte Carlo results. Regarding computational cost, the UGKWP method requires only 60 GiB of memory to simulate the three-dimensional space vehicle with 560,593 cells under various flow conditions, which is manageable even on personal workstations. Given its excellent efficiency and accuracy, the UGKWP method shows its substantial benefits in simulating multiscale flow for aerospace engineering applications.

Nomenclature

$\mathcal{A}$	=	area of cells' interfaces
C_h	=	surface heat flux coefficient
C_p	=	surface pressure coefficient
C_τ	=	surface shear stress coefficient
$\boldsymbol{c}$	=	peculiar velocity
D	=	degrees of freedom
d	=	sphere diameter
E	=	macroscopic energy
$\boldsymbol{F}$	=	fluxes for conservative variables
$\mathcal{F}$	=	time-averaged flux of the microscopic distribution function
f, g	=	gas distribution function
f_s	=	surface friction
h	=	heat flux
Kn	=	Knudsen number
L_{ref}	=	reference length
l	=	mean free path
Ma	=	Mach number
m_0	=	gas molecule mass
N_r	=	reference number of particles per cell
$\boldsymbol{n}$	=	normal direction
p	=	pressure
T	=	temperature
t	=	time
$\boldsymbol{U}$	=	macroscopic velocity
$\boldsymbol{u}$	=	particle velocity
$\boldsymbol{W}$	=	conservative variables
γ	=	specific heat ratio
Δt	=	time step
μ	=	viscosity
ρ	=	density
τ	=	relaxation time
Ω	=	volume of cells

Subscripts

Gll	=	gradient local length
i, j	=	cell index
k	=	particle index
ref	=	reference state
s	=	solid surface
w	=	wall
∞	=	freestream flow

Superscripts

eq	=	equilibrium
fr	=	freestreaming
h	=	wave part
p	=	particle part

Received 9 October 2023; revision received 3 December 2023; accepted for publication 11 January 2024; published online 12 March 2024.

*Graduate Student, Department of Mathematics; wlongab@connect.ust.hk.

†Graduate Student, Department of Mathematics; yweibe@connect.ust.hk.

‡Chair Professor/Stephen Kam Chuen Cheong Professor of Science, Department of Mathematics and Department of Mechanical and Aerospace Engineering; also HKUST Shenzhen Research Institute, Shenzhen 518057, People's Republic of China; makxu@ust.hk.

I. Introduction

MULTISCALE flows are frequently encountered in a variety of aerospace applications, including spacecraft reentry, rocket launches, and aircraft attitude control using jet flows. Experimental investigations of such problems pose challenges due to the difficulty and expense of establishing high-fidelity experimental environments, especially when attempting to replicate high-altitude atmospheric conditions. Computational fluid dynamics (CFD), a crucial tool widely used in the aerospace industry, can surmount these experimental limitations. It offers accurate and comprehensive representations of various physical quantities in evolving flowfields.

For rarefied flow simulation, the methods are mainly categorized as the deterministic method with the discretization of particle velocity space and the stochastic method with particles. Both deterministic methods [1–5] and stochastic methods [6–8] have been widely used in aerodynamic applications. However, the deterministic discrete velocity methods (DVMs) consume a significant amount of computing resources. For high-speed rarefied flow, the direct simulation Monte Carlo (DSMC) [9] method based on stochastic particles

is commonly used, such as in the calculations of shuttle orbiters, capsules, and aerospace planes in reentry problems, and has presented reliable results [10–20]. In particular, for the X38-like spacecraft, LeBeau and Lumpkin used the DSMC-based DAC software to simulate the surface pressure distribution [11] in the transitional flow regime. Li et al. [21] and Jiang [4] used the deterministic unified gas-kinetic scheme (UGKS) and stochastic DSMC to study the surface force and thermal properties of X38. It was realized that local Knudsen numbers can vary significantly around the surface of X38. In comparison with DSMC, the UGKS is a multiscale method, but its memory consumption is significantly high in high-speed flow simulation. On the other hand, the DSMC is valid in the particle mean free path and collision time scales and has difficulties in computing flow in the near-continuum regime due to the constraints on the cell size and time step. The unified gas-kinetic wave-particle (UGKWP) method takes advantage of both UGKS and DSMC and optimizes the computational efficiency and accuracy in flow studies with the co-existence of multiple flow regimes.

The UGKWP method follows the direct modeling methodology of the UGKS [22]. The UGKS is a DVM method, and its time evolution of particle distribution function is based on the coupled particle free transport and collision. With the variation of the particle collision frequency within a numerical time step, the UGKS can capture different flow physics from the free molecular flow to the NS evolution solution. The UGKS releases the restrictions on the cell size and time step being less than the particle mean free path and mean collision time. In order to improve the efficiency of UGKS in the high flow simulation, the UGKWP method replaces the discrete velocity space in UGKS with stochastic particles, overcoming the huge computational load and memory consumption of UGKS [23,24]. The wave-particle decomposition in the UGKWP method makes it possible to adjust the degrees of freedom in the computation, such as tracking all particles in the highly rarefied flow regime and evolving macroscopic flow variables in the Navier–Stokes (NS) regime. In the continuum flow regime, the UGKWP will precisely recover the gas-kinetic scheme (GKS) in the continuum flow limit [25]. Recently, the UGKWP method has been used to study the gas effect with rotational and vibrational nonequilibrium [26]. At the same time, the methodology has been used to construct multiscale methods for phonon transport [27], plasma [28], and gas-solid particle flow [29]. The current study uses the UGKWP method to simulate supersonic flow around a sphere and hypersonic flow around a space vehicle, as well as nozzle plume to vacuum and transversal jet interactions with the hypersonic flow.

This paper is organized as follows: In Sec. II, the UGKWP method based on the finite volume framework will be briefly described. In Sec. III, various multiscale flow problems will be simulated and analyzed, and the outcomes will be compared with existing experimental and simulation data to demonstrate the accuracy and efficiency of the UGKWP method. Section IV will summarize the characteristics and advantages of the UGKWP method in multiscale flows in large-scale aerodynamic applications.

II. UGKWP Method

The unified gas kinetic wave-particle (UGKWP) method is used for numerical simulations in this study. The method is constructed under the finite-volume framework. Within a discrete finite volume cell i and a discrete time step $\Delta t = t^{n+1} - t^n$, the macroscopic quantities of the flowfield $\boldsymbol{W} = (\rho, \rho\boldsymbol{U}, \rho E)$, i.e., densities of mass, momentum, and energy, are updated by the fluxes through the cell interfaces:

$$\boldsymbol{W}_i^{n+1} = \boldsymbol{W}_i^n - \frac{\Delta t}{\Omega_i} \sum_{j \in N(i)} \boldsymbol{F}_{ij} \mathcal{A}_{ij} \tag{1}$$

where Ω_i denotes the volume of cell i, $N(i)$ is the set of all interface-adjacent neighboring cells of the control volume i, and j is one of the neighboring cells, with the interface between them labeled as ij and the area denoted as $\mathcal{A}_{ij}$. $\boldsymbol{F}_{ij}$ is the time-averaged macroscopic flux crossing the interface ij.

Under the framework of the finite volume method, the key of a numerical method lies in the evolution model of the flux function through the cell interface. In the gas kinetic theory, the macroscopic flux function is obtained by taking moments of the microscopic distribution function:

$$\boldsymbol{F}_{ij} = \int \mathcal{F}_{ij} \psi \, \mathrm{d}\boldsymbol{u} \tag{2}$$

where $\psi = (1, \boldsymbol{u}, (1/2)\boldsymbol{u}^2)^T$, and $\boldsymbol{u}$ represents the microscopic particle velocity, and the time-averaged flux of the microscopic distribution function, denoted as $\mathcal{F}_{ij}$, is expressed as

$$\mathcal{F}_{ij} = \frac{1}{\Delta t} \int_0^{\Delta t} \boldsymbol{u} \cdot \boldsymbol{n}_{ij} f_{ij}(t) \, \mathrm{d}t \tag{3}$$

where $\boldsymbol{n}_{ij}$ is the unit normal vector to the interface, and $f_{ij}(t)$ represents the time-dependent distribution function on the interface. In the UGKWP method, the distribution function is described by the BGK model:

$$\frac{\partial f}{\partial t} + \boldsymbol{u} \cdot \frac{\partial f}{\partial \boldsymbol{r}} = \frac{g - f}{\tau} \tag{4}$$

Along the characteristic line, its integral solution gives the local evolution of the gas distribution function

$$f(\boldsymbol{r}, t) = \frac{1}{\tau} \int_0^t e^{-(t-t')/\tau} g(\boldsymbol{r}', t') \, \mathrm{d}t' + e^{-t/\tau} f_0(\boldsymbol{r} - \boldsymbol{u}t) \tag{5}$$

where τ is the relaxation time, $\boldsymbol{r}$ is the spatial location, $f_0(\boldsymbol{r} - \boldsymbol{u}t)$ is the initial distribution function at the beginning of each step t_n, and $g(\boldsymbol{r}', t')$ represents the local equilibrium following the Maxwell distribution:

$$g = \rho \left(\frac{\lambda}{\pi}\right)^{D/2} e^{-\lambda \boldsymbol{c}^2} \tag{6}$$

where D is the degrees of freedom of gas, and λ is related to the temperature T by $\lambda = m_0/2k_BT$. Here, m_0 and k_B are the molecular mass and Boltzmann constant, respectively. And $\boldsymbol{c} = \boldsymbol{u} - \boldsymbol{U}$ denotes the peculiar velocity.

For the numerical description of the integral solution, the UGKWP method introduces stochastic particles $\phi_k = (m_k, m_k\boldsymbol{u}_k, (1/2)m_k\boldsymbol{u}_k^2)^T$ and analytical wave $\boldsymbol{W}^h = (\rho^h, (\rho\boldsymbol{U})^h, (\rho E)^h)$ to represent the initial distribution function f_0, enhancing its ability to accurately capture nonequilibrium flows. Additionally, its adaptive wave-particle decomposition ensures efficient solutions for high-speed, multiscale flow across different flow regimes. The macroscopic flux function of the UGKWP method consists of three parts. The first part, contributed by local equilibrium state $g(\boldsymbol{r}', t')$ in the integral solution, can be directly obtained through integration

$$\boldsymbol{F}_{ij}^{\mathrm{eq}} = \int \boldsymbol{u} \cdot \boldsymbol{n}_{ij} \left[C_1 g_0 + C_2 \boldsymbol{u} \cdot \frac{\partial g}{\partial \boldsymbol{r}} + C_3 \frac{\partial g}{\partial t} \right] \psi \, \mathrm{d}\boldsymbol{u} \tag{7}$$

The second part is derived from the initial distribution function where part of freestreaming flux can be calculated analytically:

$$\boldsymbol{F}_{ij}^{\mathrm{fr},h} = \int \boldsymbol{u} \cdot \boldsymbol{n}_{ij} \left[C_4 g_0 + C_5 \boldsymbol{u} \cdot \frac{\partial g}{\partial \boldsymbol{r}} \right] \psi \, \mathrm{d}\boldsymbol{u} \tag{8}$$

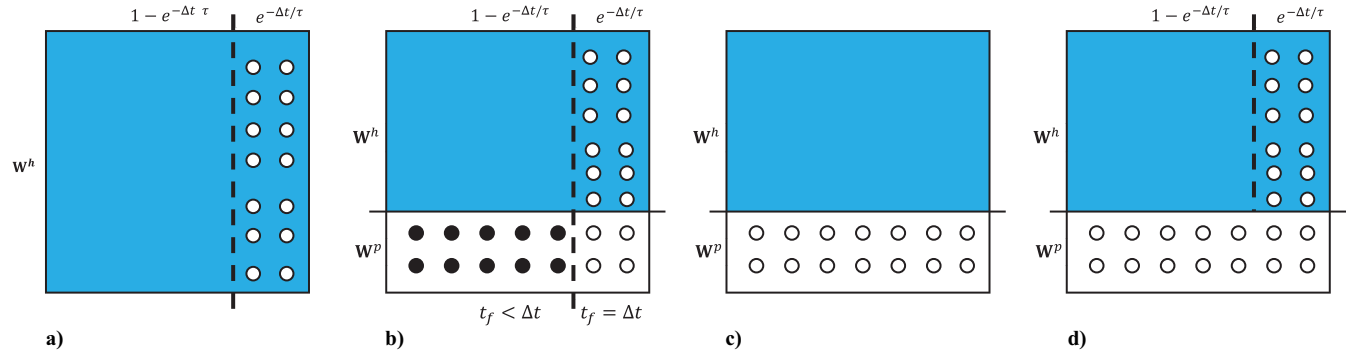

Fig. 1 Diagram to illustrate the composition of the particles during time evolution in the UGKWP method. (a) Initial field, (b) classification of the collisionless and collisional particles for W_i^p, (c) update on the macroscopic level, and (d) update on the microscopic level.

Therefore, $\boldsymbol{F}_{ij}^{\mathrm{eq}}$ and $F_{ij}^{\mathrm{fr},h}$ are regarded as analytical waves, where C_1, C_2, C_3, C_4, and C_5 are corresponding coefficients:

$$
\begin{aligned}
C_1 &= 1-\frac{\tau}{\Delta t}\left(1-e^{-\Delta t/\tau}\right),\\
C_2 &= -\tau+\frac{2\tau^2}{\Delta t}-e^{-\Delta t/\tau}\left(\frac{2\tau^2}{\Delta t}+\tau\right),\\
C_3 &= \frac{1}{2}\Delta t-\tau+\frac{\tau^2}{\Delta t}\left(1-e^{-\Delta t/\tau}\right),\\
C_4 &= \frac{\tau}{\Delta t}\left(1-e^{-\Delta t/\tau}\right)-e^{-\Delta t/\tau},\\
C_5 &= \tau e^{-\Delta t/\tau}-\frac{\tau^2}{\Delta t}\left(1-e^{-\Delta t/\tau}\right)+\frac{1}{2}\Delta t e^{-\Delta t/\tau}
\end{aligned}
\tag{9}
$$

The third part of macroscopic flux is contributed by particle free transport $\boldsymbol{W}_i^{\mathrm{fr}}$, which is obtained by tracking the discrete particles crossing the interface:

$$
\boldsymbol{W}_i^{\mathrm{fr}}=\frac{1}{\Delta t}\left(\sum_{\boldsymbol{x}_k\in\Omega_i}\boldsymbol{\phi}_k-\sum_{\boldsymbol{x}_k^n\in\Omega_i}\boldsymbol{\phi}_k\right) \tag{10}
$$

where $\boldsymbol{x}_k^n$ denotes the position of kth particle at initial time t^n, and $\boldsymbol{x}_k$ is the position of the particle after free transport. After deriving macroscopic flux on the cell interface, the cell-averaged macroscopic variable $\boldsymbol{W}_i$ is updated by

$$
\boldsymbol{W}_i^{n+1}=\boldsymbol{W}_i^n-\frac{\Delta t}{\Omega_i}\sum_{j\in N(i)}\boldsymbol{F}_{ij}^{\mathrm{eq}}\mathcal{A}_{ij}-\frac{\Delta t}{\Omega_i}\sum_{j\in N(i)}\boldsymbol{F}_{ij}^{\mathrm{fr},h}\mathcal{A}_{ij}+\frac{\Delta t}{\Omega_i}\boldsymbol{W}_i^{\mathrm{fr},p} \tag{11}
$$

The wave-particle decomposition process is reflected at the start and end of each time step in Fig. 1. At the beginning of the update, random particles are sampled to separate them from the macroscopic waves. After the update, particles with free transport time less than the time step Δt are removed and absorbed into the macroscopic waves. For a detailed introduction to the UGKWP method, please refer to references [23,24,30,31].

III. Flow Studies and Discussion

The UGKWP method can simulate flow in all flow regimes with great efficiency and accuracy. Its wave-particle decomposition takes a significant advantage in three-dimensional flow, especially for hypersonic one around complex geometry, unsteady nozzle plume flow to background vacuum, and hypersonic side-jet interaction. The method can greatly reduce memory consumption and improve computation efficiency. This section will show the numerical simulation results of the UGKWP method in many cases. Detailed comparisons of the key flow structures will be presented, such as the aerodynamic force and aerothermal distribution of the high-speed flow around the space vehicle, the axial pressure and temperature of the nozzle plume, as well as the flow separation, reattachment, and penetration phenomena in the side-jet interaction. Combined with computational time, memory occupation, and other computational performance, this section will fully demonstrate the great potential of the UGKWP method in simulating the multiscale flow in large-scale engineering applications.

The Knudsen number is used to describe the degree of rarefaction in multiscale flows. In the nonequilibrium flow, the gradient-length-dependent local Knudsen number Kn_{Gll} is used to reveal the local nonequilibrium:

$$
Kn_{\mathrm{Gll}}=\frac{l}{\rho/|\nabla\rho|} \tag{12}
$$

where l is the local average molecular free path.

For the initial condition, the Knudsen number of freestream flow Kn_∞ is adopted to define a case:

$$
Kn_\infty=\frac{l_\infty}{L_{\mathrm{ref}}} \tag{13}
$$

where l_∞ is the mean free path of molecules of the freestream flow, and L_{ref} is the reference length for defining the Knudsen number Kn_∞. The density of the specific gas can be obtained based on the Knudsen number of the freestream flow:

$$
\rho_\infty=\frac{4\alpha(5-2\omega)(7-2\omega)}{5(\alpha+1)(\alpha+2)}\sqrt{\frac{m}{2\pi k_B T_\infty}}\frac{\mu_\infty}{L_{\mathrm{ref}}Kn_\infty} \tag{14}
$$

where m represents the molecular mass. The dynamic viscosity is determined by a power law:

$$
\mu=\mu_{\mathrm{ref}}\left(\frac{T}{T_{\mathrm{ref}}}\right)^{\omega} \tag{15}
$$

The gas internal degrees of freedom in the Maxwell distribution Eq. (6) are calculated based on the specific heat ratio:

$$
D=\frac{2}{\gamma-1} \tag{16}
$$

Table 1 provides the gas parameters used in this study. Note that the reference dynamic viscosity is defined at a reference temperature

Table 1 Gas and physical property parameters used in this study

Gas	Case	m, kg	μ_{ref}, N · s · m^{-2}	ω	α	γ
N_2	Sphere, side jet	4.65×10^{-26}	1.65×10^{-5}	0.74	1.0	1.4
Ar	X38	6.63×10^{-26}	2.12×10^{-5}	0.81	1.0	1.67
CO_2	Nozzle	7.31×10^{-26}	1.38×10^{-5}	0.67	1.0	1.4

$T_{\text{ref}} = 273$ K. A simplified CO_2 molecular model without vibration mode is employed, and all internal degrees of freedom are resolved by the Maxwell distribution.

The current UGKWP method can handle structured, unstructured, and hybrid meshes for different numerical cases. The corresponding particle tracking and sampling technique are demonstrated by earlier work [24].

In addition, all cases in this work are simulated by the explicit UGKWP method with the CFL number 0.95. The spatial reconstruction of macroscopic flow variables is carried out by the least-square method with the Venkatarishnan limiter [32].

A. Supersonic Flow Around a Sphere

A supersonic flow passing over a three-dimensional sphere at Mach number 4.25 is simulated for various Knudsen numbers using nitrogen gas. To define the Knudsen number, the reference length is chosen as the diameter of the sphere, i.e., $d = 0.002$ m. The physical domain, consisting of 3456×40 hexahedral cells, is illustrated in Fig. 2, together with a detailed view of the mesh near the solid surface, where the height of the first layer cell is $0.005d$. Table 2 presents the initial conditions of the cases tested, including Knudsen number, density, and temperature of the freestream flow, as well as the altitude estimated by density. The simulation adopts supersonic far-field inflow and outflow conditions, and an isothermal wall at the sphere surface with a temperature of the freestream flow. The reference number of particles sampled per cell in the UGKWP method is set to 100 for all cases.

Table 3 presents the drag coefficients computed by the UGKWP method, along with the corresponding errors compared to experimental results. All errors are less than or nearly 1%. As the freestream flow becomes more rarefied, the drag force on the sphere increases.

Figures 3–7 depict the distribution of density, temperature, Mach number, and gradient-length-dependent local Knudsen number in the flowfield simulated by UGKWP. An increase in the thickness of the bow shock in front of the sphere is observed as the Knudsen number increases. The local Knudsen number distribution reveals strong nonequilibrium effects in the leeward area of the sphere and within the shock.

The maximum and minimum gradient-length-dependent local Knudsen numbers are given in Table 4, which illustrates that all cases involve multiscale flow with nonequilibrium effects. $Kn_{\text{Gll,max}}$ are above 10, and more than 6 orders of magnitude greater than $Kn_{\text{Gll,min}}$. $Kn_{\text{Gll,max}}$ reaches a peak value of 2.31×10^5 at $Kn_\infty = 0.672$, illustrating the existence of strong nonequilibrium effects. As the Knudsen number in freestream flow falls, the nonequilibrium and multiscale effects both diminish.

Table 2 Freestream flow parameters of supersonic flow at $Ma_\infty = 4.25$ around a sphere

Kn_∞	Altitude, km	ρ_∞, kg/(m^3 · s)	T_∞, K	T_w, K
0.672	89.1	3.173×10^{-5}	65.04	302
0.338	83.3	6.313×10^{-5}	65.04	302
0.121	74.7	1.761×10^{-4}	65.04	302
0.080	71.1	2.675×10^{-4}	65.04	302
0.031	63.2	6.879×10^{-4}	65.04	302

Table 3 Comparison of the drag coefficients for supersonic flow at $Ma_\infty = 4.25$ over a sphere

		Drag coefficient (error)		
Ma_∞	Kn_∞	Experiment (air)	UGKS (N_2)	UGKWP (N_2)
4.25	0.672	2.42	2.356 (−2.64%)	2.423 (0.13%)
4.25	0.338	2.12	2.101 (−0.87%)	2.114 (−0.30%)
4.25	0.121	1.69	1.694 (+0.23%)	1.671 (−1.12%)
4.25	0.080	1.53	1.558 (1.80%)	1.527 (−0.23%)
4.25	0.031	1.35	1.355 (0.39%)	1.352 (0.12%)

Figure 8 illustrates the distribution of pressure, shear stress, and heat flux coefficients on the solid surface. The pressure and shear stress coefficients exhibit excellent agreement with DSMC data from the study by Zhang et al. [3]. However, the heat flux on the windward side of the sphere deviates from the reference data, most likely due to differences in the Prandtl number. In this case, the surface coefficients are nondimensionalized as follows:

$$C_p = \frac{p_s - p_\infty}{(1/2)\rho_\infty U_\infty^2}, \quad C_\tau = \frac{f_s}{(1/2)\rho_\infty U_\infty^2}, \quad C_h = \frac{h_s}{(1/2)\rho_\infty U_\infty^3} \tag{17}$$

where p_s is the surface pressure, p_∞ is the pressure in freestream flow, f_s is the surface friction, and h_s is the surface heat flux.

The computational efficiency and resource consumption of the simulations are shown in Table 5, which are conducted on the

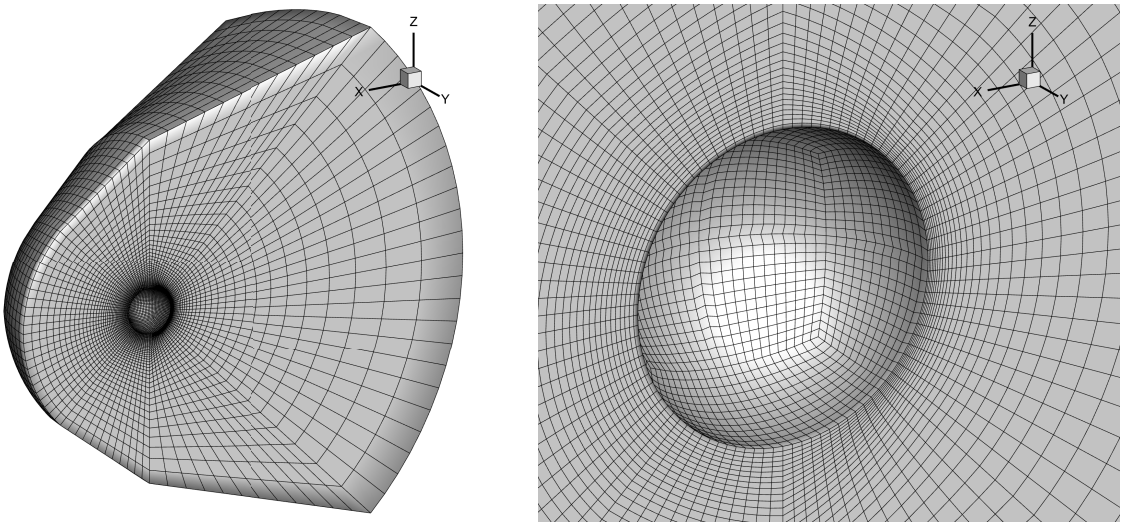

a) b)

Fig. 2 Physical domain of supersonic flow around a sphere that consists of 138,240 hexahedral cells. a) The entire domain, and b) detailed mesh distribution in the vicinity of the solid surface.

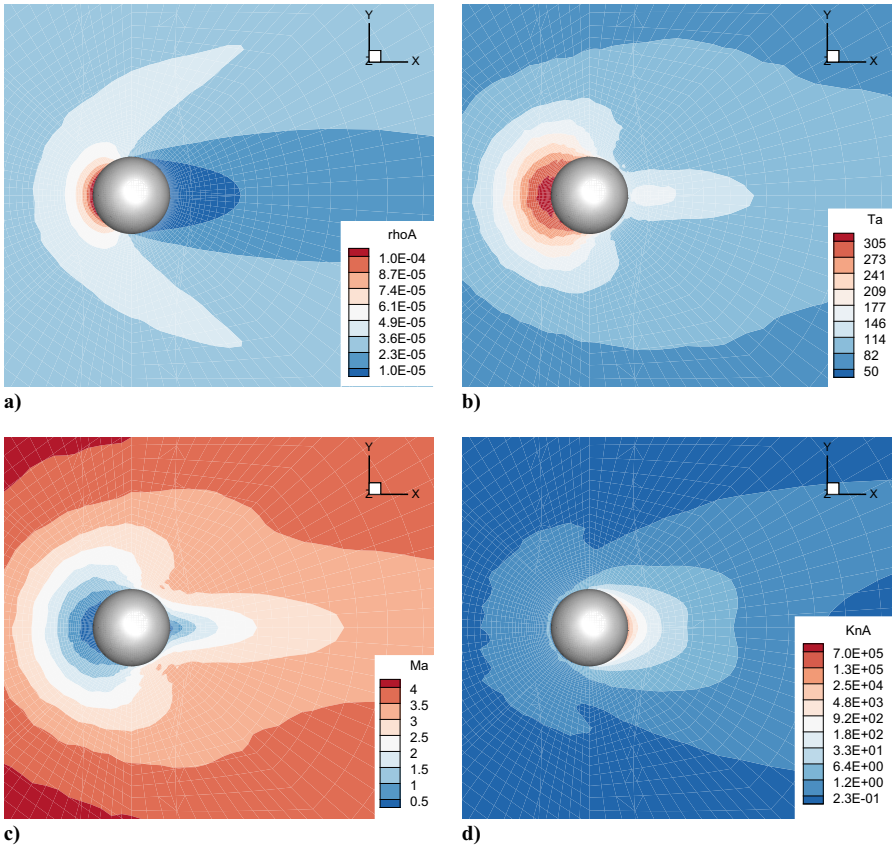

Fig. 3 Supersonic flow around a sphere at $Ma_\infty = 4.25$ and $Kn_\infty = 0.672$ by the UGKWP method. a) Density, b) temperature, c) Mach number, and d) local Knudsen number contours.

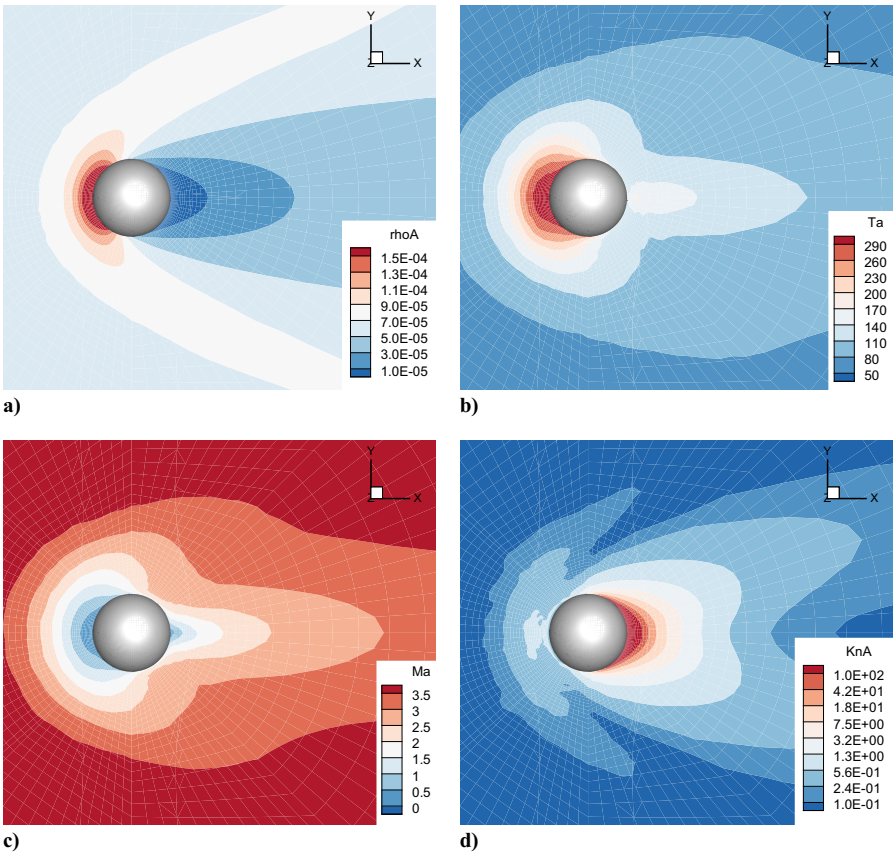

Fig. 4 Supersonic flow around a sphere at $Ma_\infty = 4.25$ and $Kn_\infty = 0.338$ by the UGKWP method. a) Density, b) temperature, c) Mach number, and d) local Knudsen number contours.

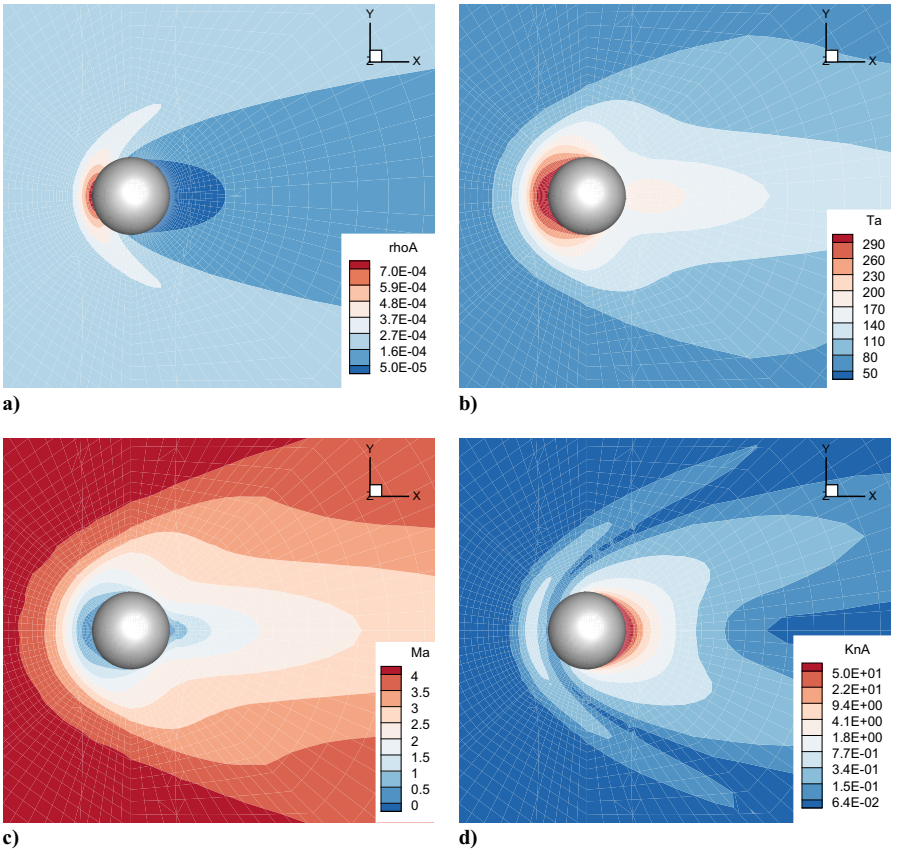

Fig. 5 Supersonic flow around a sphere at $Ma_\infty = 4.25$ and $Kn_\infty = 0.121$ by the UGKWP method. a) Density, b) temperature, c) Mach number, and d) local Knudsen number contours.

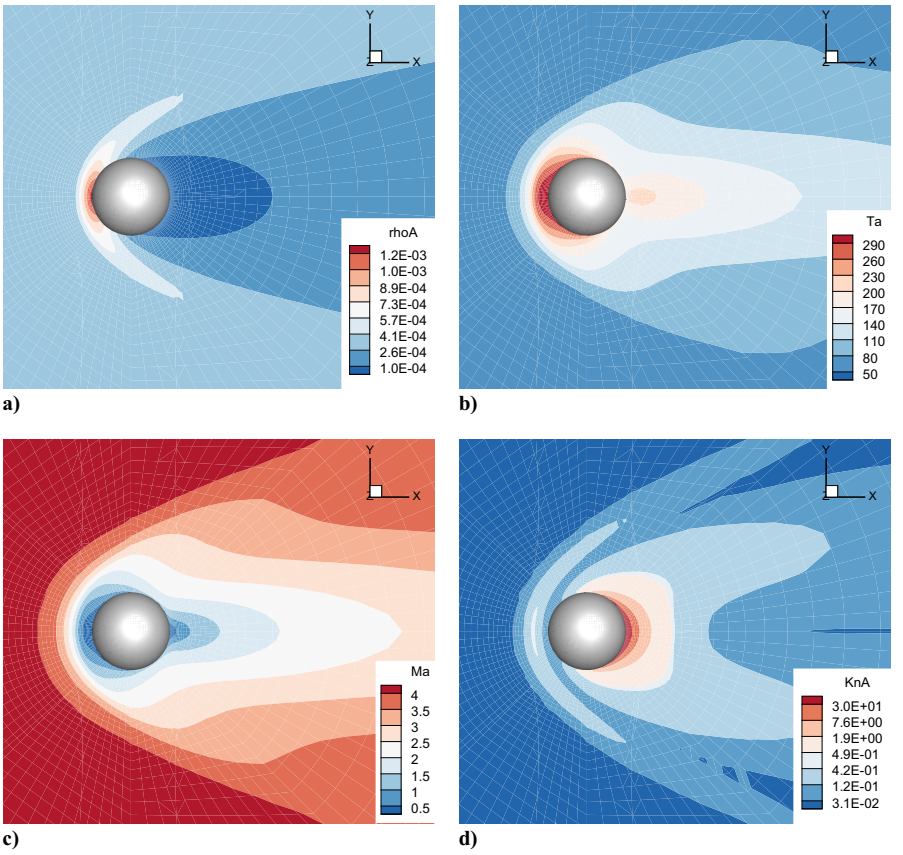

Fig. 6 Supersonic flow around a sphere at $Ma_\infty = 4.25$ and $Kn_\infty = 0.080$ by the UGKWP method. a) Density, b) temperature, c) Mach number, and d) local Knudsen number contours.

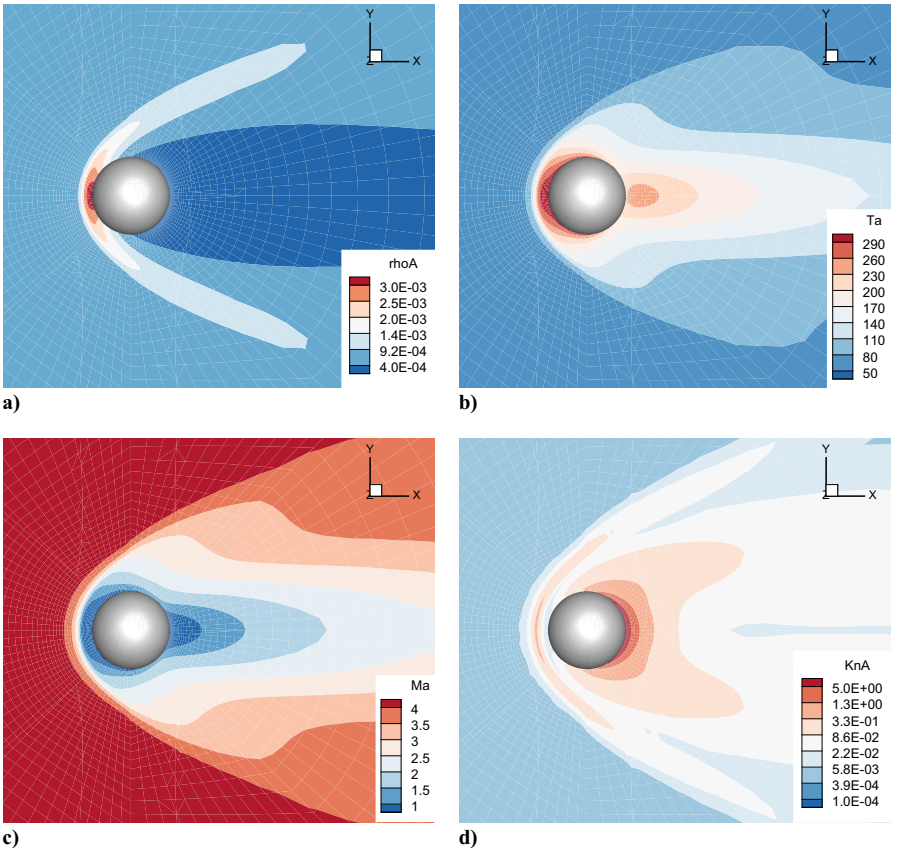

Fig. 7 Supersonic flow around a sphere at $Ma_\infty = 4.25$ and $Kn_\infty = 0.031$ by the UGKWP method. a) Density, b) temperature, c) Mach number, and d) local Knudsen number contours.

Table 4 Supersonic flow at $Ma_\infty = 4.25$ around a sphere

Kn_∞	$Kn_{\mathrm{Gll,min}}$	$Kn_{\mathrm{Gll,max}}$	$\log \frac{Kn_{\mathrm{Gll,max}}}{Kn_{\mathrm{Gll,min}}}$
0.672	4.06×10^{-3}	2.31×10^{5}	7.75
0.338	1.06×10^{-3}	2.36×10^{4}	7.35
0.121	5.22×10^{-4}	1.04×10^{3}	6.30
0.080	2.01×10^{-4}	3.05×10^{2}	6.18
0.031	2.03×10^{-5}	3.07×10	6.17

Maximum and minimum gradient-length-dependent local Knudsen numbers.

SUGON computation platform with a CPU model of 7285 32C 2.0 GHz. Time-averaging begins after 12,000 steps, with a variation of averaging steps. Steady states are achieved with fewer averaging steps in rarefied cases. In the near-continuous cases, few particles will emerge in the wave-particle decomposition. The case at Knudsen number of 0.121 has the highest computational cost due to the large number of particles sampled and removed in a single time step with the dynamic wave-particle decomposition. In the current study, UGKWP exhibits high computational efficiency and consumes minimal memory resources in comparison with DVM methods, and it has particular advantages in approaching the limiting solutions of continuum and free molecular flow in a single computation.

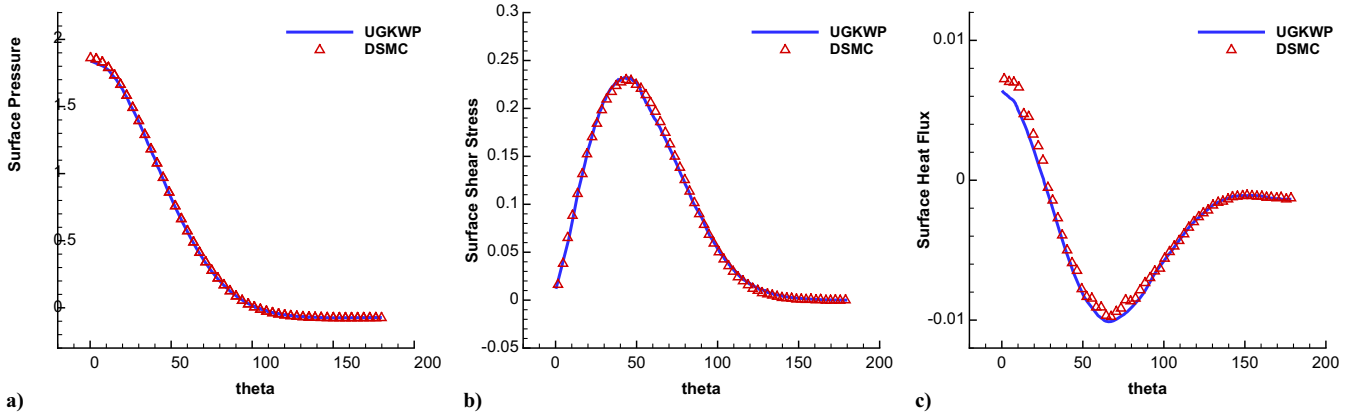

Fig. 8 Surface quantities on a sphere at $Ma_\infty = 4.25$ and $Kn_\infty = 0.031$ by the UGKWP method. a) Surface pressure coefficient C_p, b) surface shear stress coefficient C_τ, and c) surface heat flux coefficient C_h.

Table 5 Computational cost for simulations of the supersonic flow around a sphere at $Ma_\infty = 4.25$ by the UGKWP method

Kn_∞	Computation steps	Wall clock time, h	Cores	Estimated memory, GiB
0.672	12,000 + 500[a]	4.64	128	2.12
0.338	12,000 + 1,000[a]	5.75	128	2.01
0.121	12,000 + 3,500[a]	6.08	128	1.74
0.080	12,000 + 4,000[a]	4.63	128	1.56
0.031	12,000 + 13,000[a]	3.46	128	1.40

The physical domain consists of 138,240 cells, and the reference number of particles per cell in the UGKWP method is set as $N_r = 100$.
[a]Steps of time-averaging process in the UGKWP simulations.

Table 6 Freestream flow parameters of hypersonic flow at $Ma_\infty = 8.0$ around an X38-like vehicle

Kn_∞	AoA, °	Altitude, km	ρ, kg/(m^3 · s)	T_∞, K	T_w, K
2.75	0	136.8	1.11×10^{-7}	56	300
0.275	0	117.4	1.11×10^{-6}	56	300
0.0275	0	98.0	1.11×10^{-5}	56	300
0.00275	0	78.6	1.11×10^{-4}	56	300
2.75	20	136.8	1.11×10^{-7}	56	300
0.275	20	117.4	1.11×10^{-6}	56	300
0.0275	20	98.0	1.11×10^{-5}	56	300
0.00275	20	78.6	1.11×10^{-4}	56	300

B. Hypersonic Flow Around X38-Like Space Vehicle

Simulations of hypersonic flows at $Ma_\infty = 8.0$ in all flow regimes passing over an X38-like space vehicle at angles of attack of AoA = 0° and AoA = 20°, are conducted with Argon gas. The geometry of the space vehicle used in the simulations is depicted in Fig. 9. The unstructured symmetry mesh used is shown in Fig. 10, consisting of 560,593 cells with no surface refinement for most cases. For the case of Knudsen number 0.00275, a refined mesh in the vicinity of the solid surface is adopted to obtain more accurate results of surface quantities, with a reduction of the cell height of the first layer to 0.1 of the original cell height.

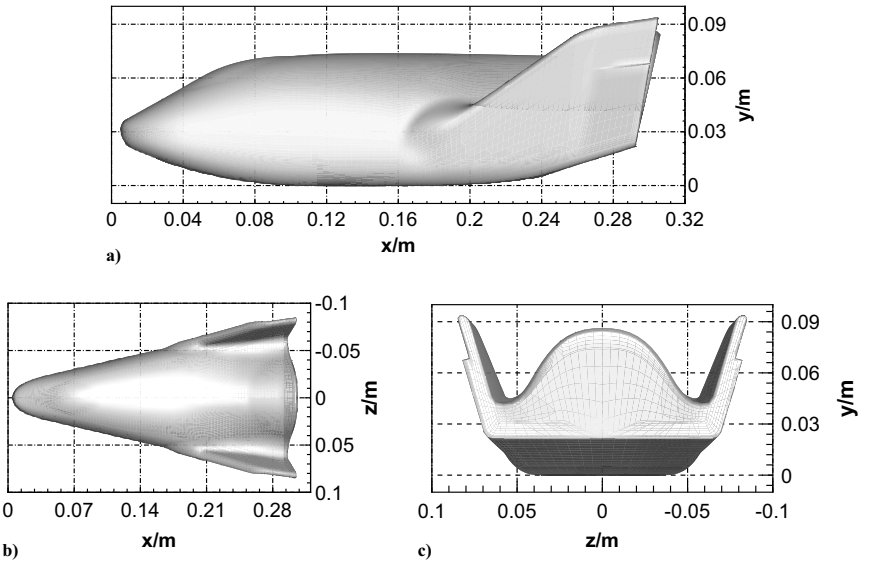

Fig. 9 Sketch of the X38-like space vehicle.

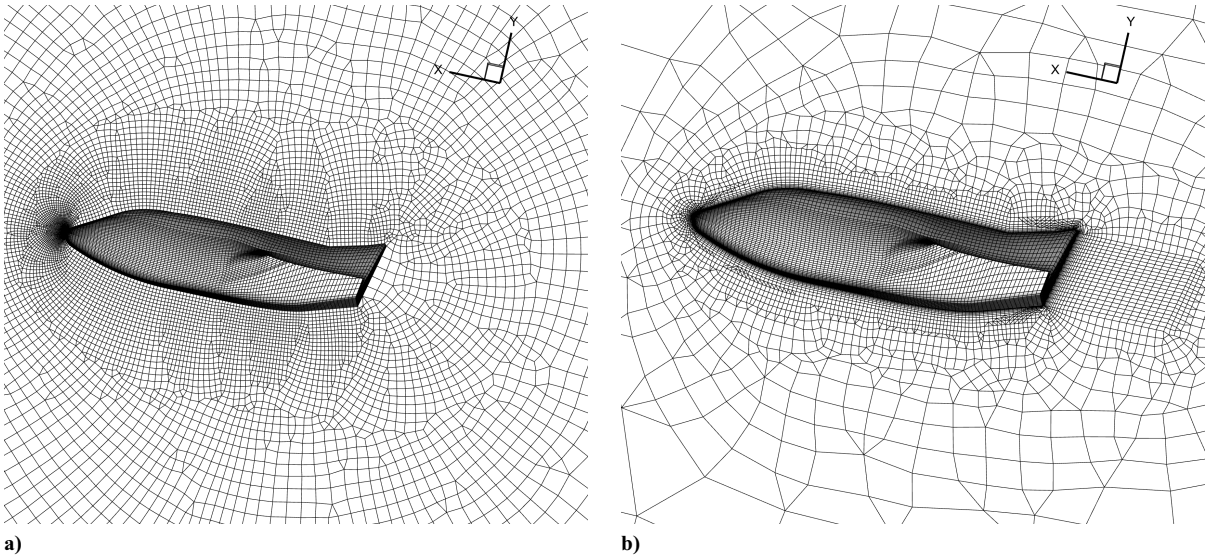

Fig. 10 Three-dimensional physical meshes of hypersonic flow at $Ma_\infty = 8.0$ around an X38-like space vehicle. Domain consists of a) 560,593 cells and b) 246,558 cells.

Table 7 Comparison of the drag coefficients for hypersonic flow at $Ma_\infty = 8.0$ over an X38-like vehicle

			Drag coefficient (error)		
Ma_∞	Kn_∞	AoA, °	DSMC	UGKS	UGKWP
8.0	0.00275	20	0.297	0.289 (−2.64%)	0.294 (−1.28%)
8.0	0.0275	20	0.536	0.556 (3.73%)	0.520 (−2.94%)
8.0	0.275	20	0.979	1.002 (2.35%)	0.989 (1.00%)
8.0	2.75	20	1.187	1.209 (0.02%)	1.209 (0.02%)
8.0	0.00275	0	0.227	— —	0.229 (0.90%)
8.0	0.0275	0	0.463	— —	0.457 (−1.30%)
8.0	0.275	0	0.833	— —	0.803 (−3.58%)
8.0	2.75	0	0.937	— —	0.943 (0.61%)

The flow conditions of all cases are listed in Table 6. To determine the Knudsen number of the freestream flow and for the nondimensionalization procedure, the characteristic length and area of the vehicle are chosen as 0.28 m and 0.012 m^2, respectively. The Knudsen number is calculated from the freestream flow density by the hard-sphere model, varying from 0.00275 to 2.75, which covers flow regimes from near continuum flow to free molecule one. The third column is the corresponding altitude estimated by the free-steam flow density.

Drag coefficients at AoA = 0° and AoA = 20° are presented in Table 7. The drag coefficients increase dramatically for all cases as the flow becomes rarefied. The UGKWP method simulated results agree well with DSMC and UGKS data in Ref. [21].

Distributions of density, Mach number, temperature, and local Knudsen number of all cases are illustrated. Figures 11–14 show the simulation results at AoA = 0° in different flow regimes, while Figs. 15–18 give contours at AoA = 20°. The density contours at different Knudsen numbers show the high density in the windward region and low density in the leeward region and present the multiple-scale flow structure in all cases. The local Knudsen number distributions show strong nonequilibrium effects in the vicinity of the vehicle tail. From the Mach number distributions, shock and discontinuous flow structures can be observed in Fig. 11b for $Kn_\infty = 0.00275$. At $Kn_\infty = 2.75$, Fig. 14b shows there is no clear discontinuity in the windward region. As the Knudsen number in the freestream flow rises, the sharp shock wave in the windward region gets thicker and weaker, and merges together with the boundary layer to form a diffusive structure.

Figure 19 depicts the gradient-length-dependent local Knudsen number Kn_{GII} on the solid surface with AoA = 20°. For all Kn_∞, the Kn_{GII} reaches its peak at the edge of the leeward region, which is 5–6 orders of magnitude higher than the lowest value. As the Kn_∞ increases, the peak value rises significantly, leading to more areas with a nonequilibrium effect on the solid surface.

Figures 20–22 show the distributions of surface physical quantities at the symmetrical section for all cases with AoA = 20°. The pressure coefficients C_p, heat flux coefficients C_h and shear stress coefficients C_τ are normalized by density ρ_∞ and velocity U_∞ of freestream flow:

$$C_p = \frac{p_s}{(1/2)\rho_\infty U_\infty^2}, \quad C_\tau = \frac{f_s}{(1/2)\rho_\infty U_\infty^2}, \quad C_h = \frac{h_s}{(1/2)\rho_\infty U_\infty^3} \tag{18}$$

The peak values are concentrated near the nose of the vehicle, and decrease as the Knudsen number falls, which indicates the significant nonequilibrium in the rarefied regime. Comparing the maximum value of surface quantities at $Kn_\infty = 0.00275$ and $Kn_\infty = 2.75$, surface pressure decreases from near 3 to 2, and heat flux diminishes from over 1 to less than 1/3, while surface friction is reduced to nearly 1/5. Due to flat-plate-like geometry, coefficients on the lower surface of the model are almost constant at 0. Although statistical scatter can

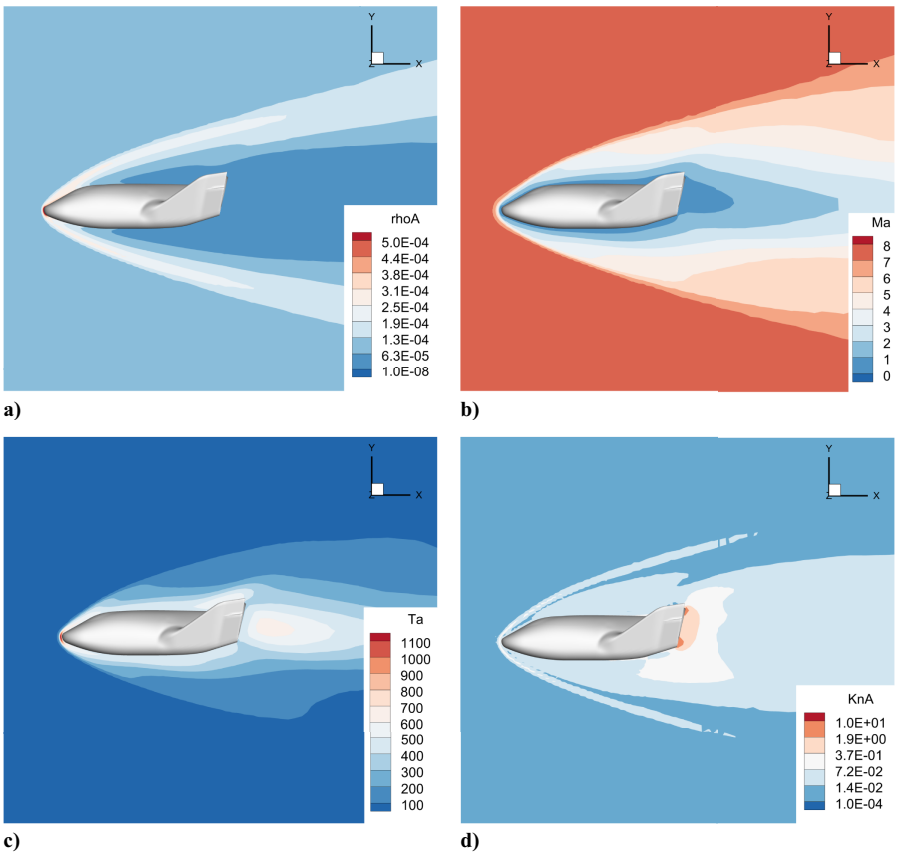

Fig. 11 Hypersonic flow around an X38-like vehicle at $Ma_\infty = 8.0$ with AoA = 0° and $Kn_\infty = 0.00275$ by the UGKWP method. a) Density, b) temperature, c) Mach number, and d) local Knudsen number contours.

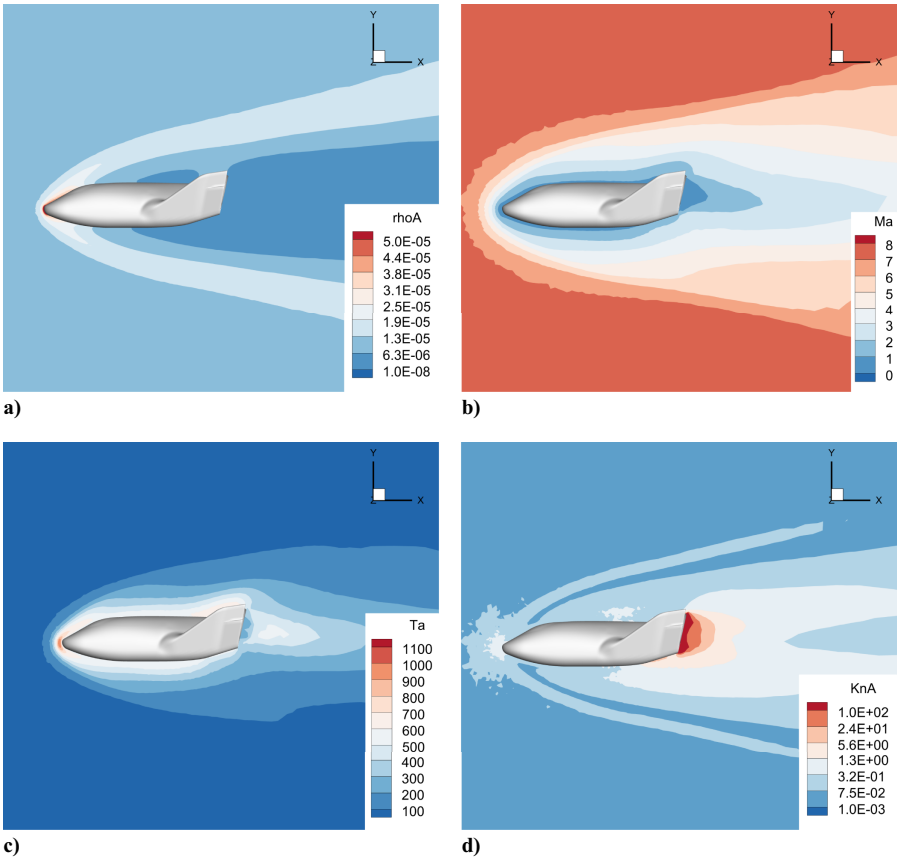

Fig. 12 Hypersonic flow around an X38-like vehicle at $Ma_\infty = 8.0$ with AoA $= 0°$ and $Kn_\infty = 0.0275$ by the UGKWP method. a) Density, b) temperature, c) Mach number, and d) local Knudsen number contours.

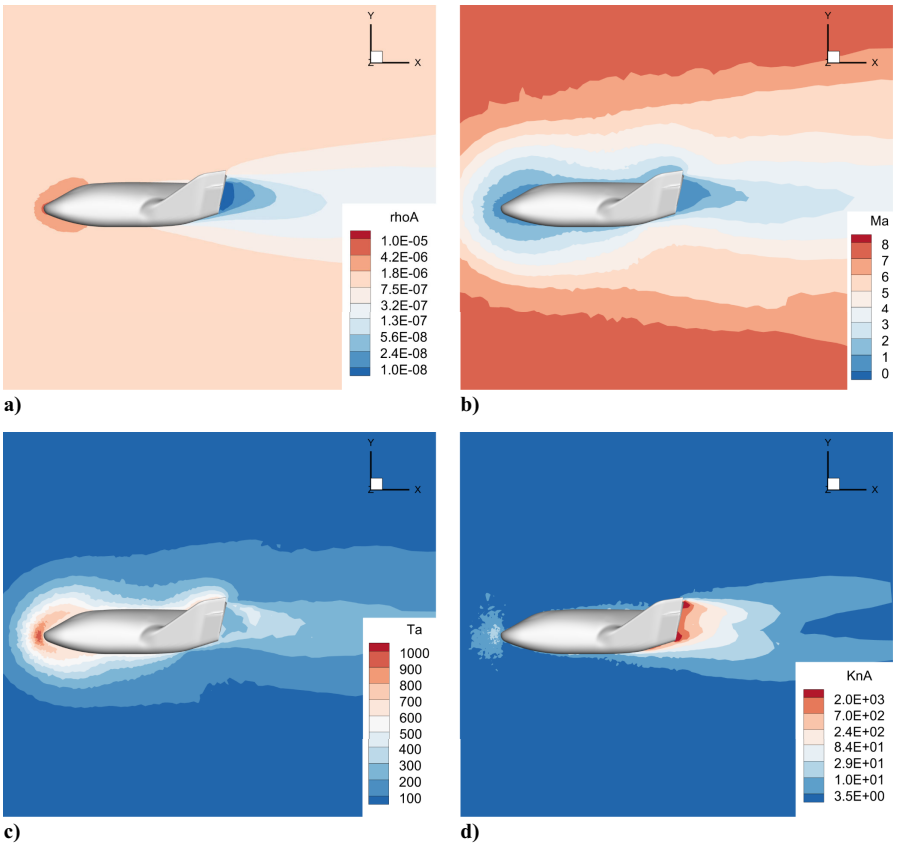

Fig. 13 Hypersonic flow around an X38-like vehicle at $Ma_\infty = 8.0$ with AoA $= 0°$ and $Kn_\infty = 0.275$ by the UGKWP method. a) Density, b) temperature, c) Mach number, and d) local Knudsen number contours.

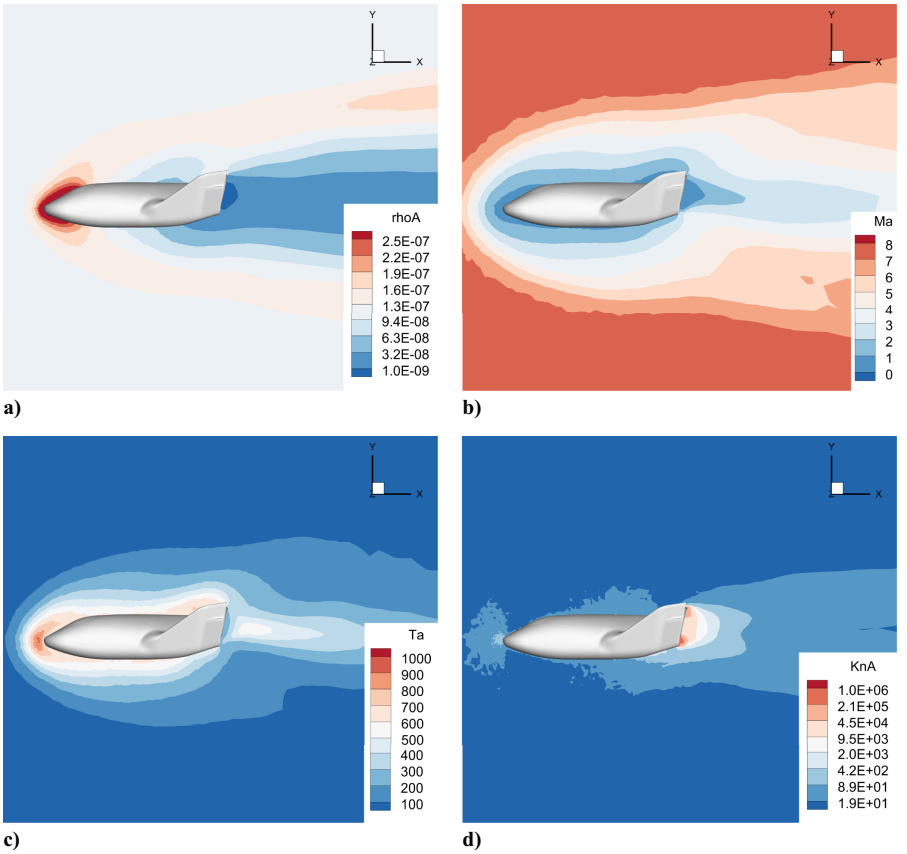

Fig. 14 Hypersonic flow around an X38-like vehicle at $Ma_\infty = 8.0$ with AoA $= 0°$ and $Kn_\infty = 2.75$ by the UGKWP method. a) Density, b) temperature, c) Mach number, and d) local Knudsen number contours.

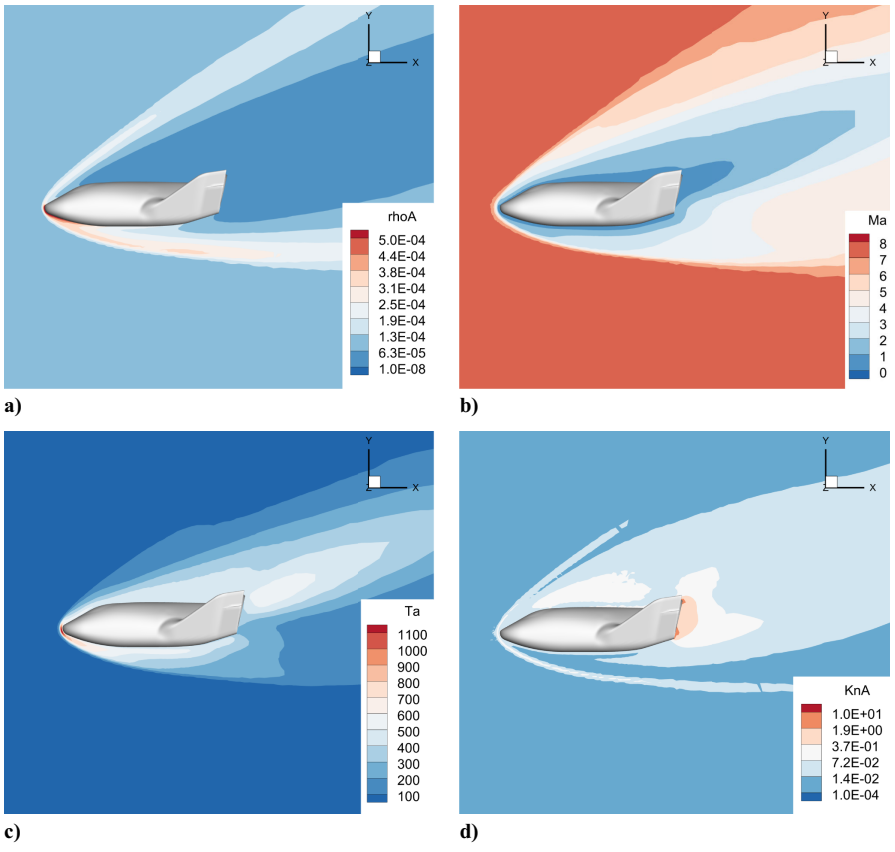

Fig. 15 Hypersonic flow around an X38-like vehicle at $Ma_\infty = 8.0$ with AoA $= 20°$ and $Kn_\infty = 0.00275$ by the UGKWP method. a) Density, b) temperature, c) Mach number, and d) local Knudsen number contours.

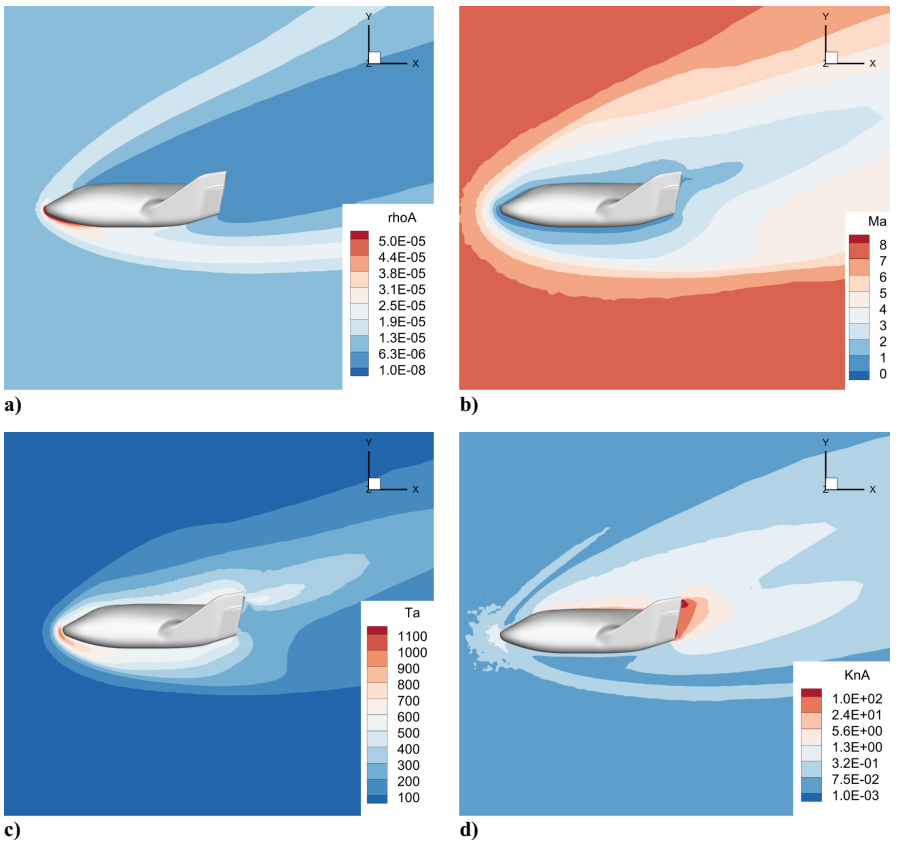

Fig. 16 Hypersonic flow around an X38-like vehicle at $Ma_\infty = 8.0$ with AoA $= 20^\circ$ and $Kn_\infty = 0.0275$ by the UGKWP method. a) Density, b) temperature, c) Mach number, and d) local Knudsen number contours.

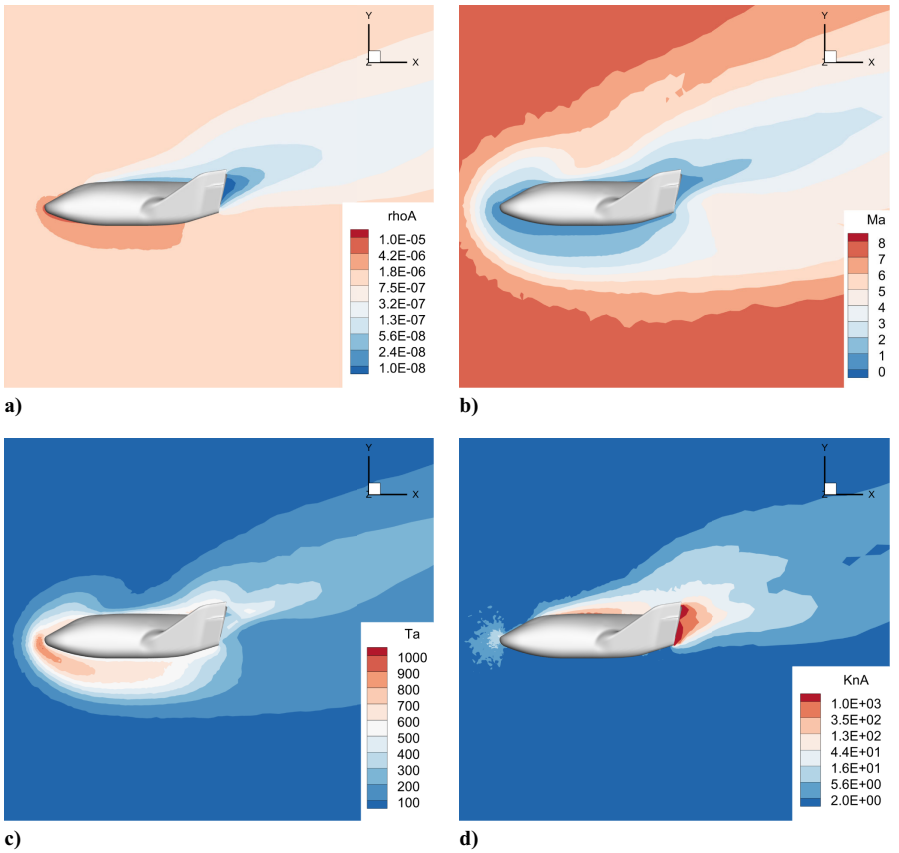

Fig. 17 Hypersonic flow around an X38-like vehicle at $Ma_\infty = 8.0$ with AoA $= 20^\circ$ and $Kn_\infty = 0.275$ by the UGKWP method. a) Density, b) temperature, c) Mach number, and d) local Knudsen number contours.

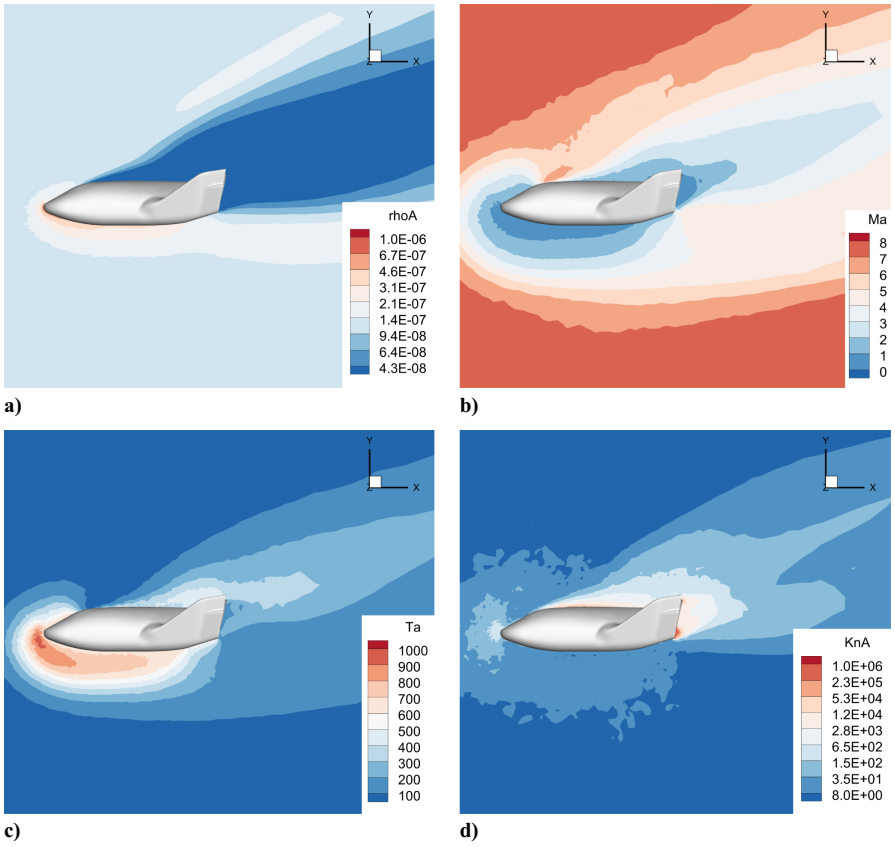

Fig. 18 Hypersonic flow around an X38-like vehicle at $Ma_\infty = 8.0$ with AoA $= 20^\circ$ and $Kn_\infty = 2.75$ by the UGKWP method. a) Density, b) temperature, c) Mach number, and d) local Knudsen number contours.

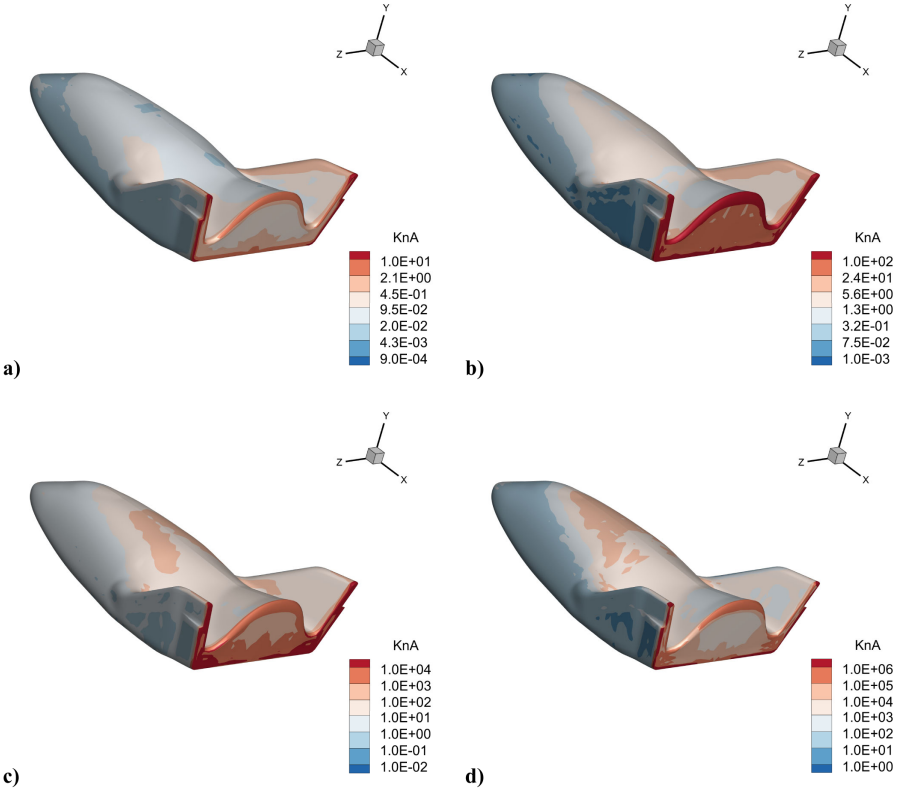

Fig. 19 Hypersonic flow around an X38-like vehicle at $Ma_\infty = 8.0$ with AoA $= 20^\circ$ by the UGKWP method. The local Knudsen number Kn_{GII} distributions on the solid surface at a) $Kn_\infty = 0.00275$, b) $Kn_\infty = 0.0275$, c) $Kn_\infty = 0.275$, and d) $Kn_\infty = 2.75$.

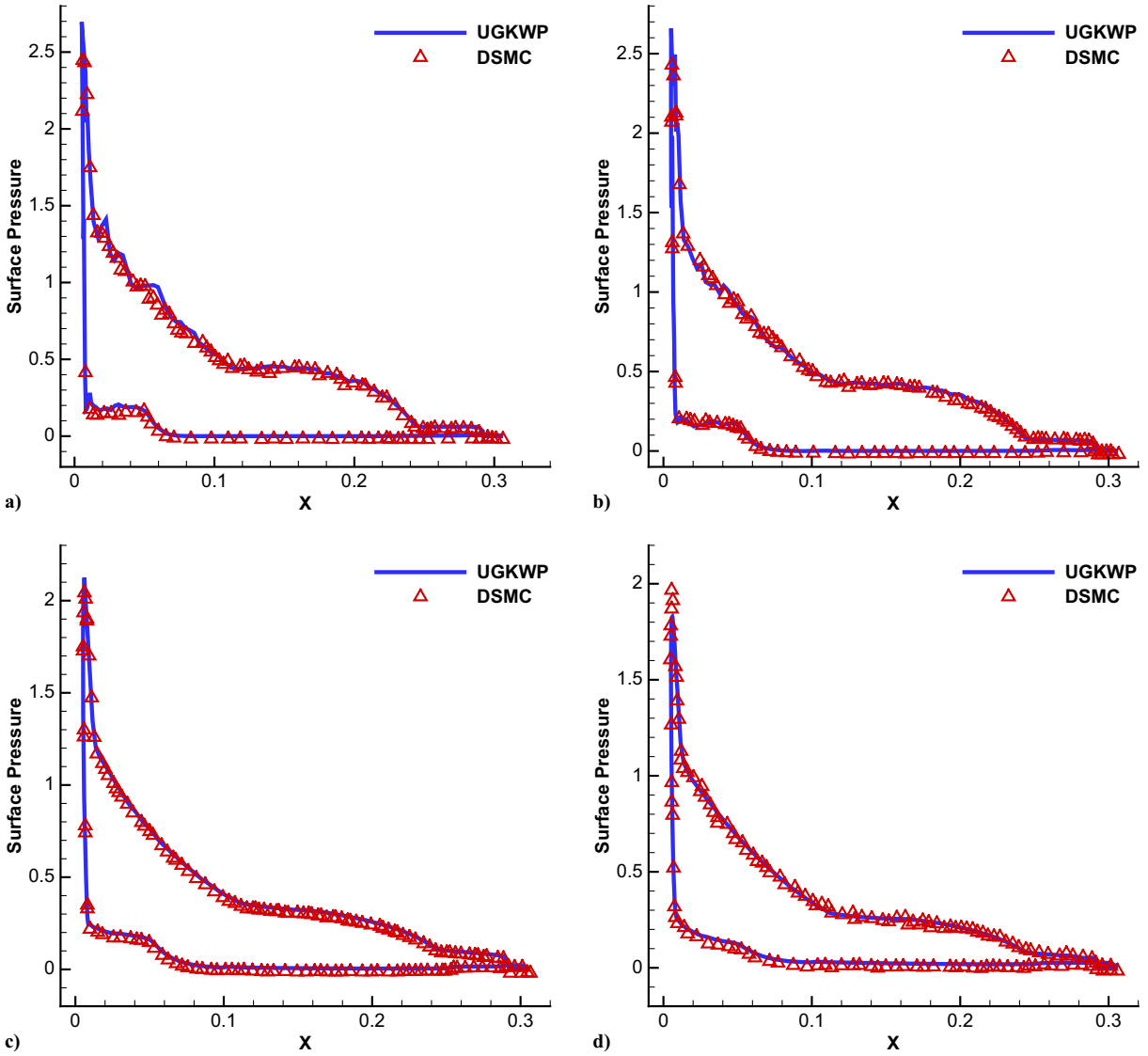

Fig. 20 Pressure coefficients on the axial surface of X38-like vehicle at $Ma_\infty = 8.0$ with AoA $= 20°$ by the UGKWP method. a) $Kn_\infty = 2.75$, b) $Kn_\infty = 0.275$, c) $Kn_\infty = 0.0275$, and d) $Kn_\infty = 0.00275$.

be observed in the case at $Kn_\infty = 2.75$, all coefficients agree well with DSMC data.

Table 8 gives the computational efficiency and the consumption of computational resources for AoA $= 0°$ and AoA $= 20°$. All the calculations are taken on the SUGON computation platform, CPU model used is 7285H 32C 2.5 GHz. Simulations start averaging after 40,000 steps and reach a steady state after varying averaging steps. For cases at $Kn_\infty = 0.00275$, it consumes dramatically less memory and costs due to the reduction of particles in the wave-particle decomposition. However, for cases at $Kn_\infty = 0.0275$, even though the initially sampled particle number is smaller compared with rarefied cases, the competitive decomposition of wave-particle and the relatively large number of particles removed and resampled in each step consume more memory. The tendency of the simulation costs in all cases agrees with that observed in the sphere case.

C. Nozzle Plume Expanding into a Vacuum

In this section, a carbon dioxide nozzle plume expanding to an extreme vacuum background is simulated. The geometric shape of the nozzle is based on the model used in Boyd et al. [33], as shown in Fig. 23. Inside the nozzle, the Knudsen number of the flow is small enough to approach the continuum flow regime. In the outer backflow and plume regions, the Knudsen number gets to the free molecule regime. This multiscale problem poses great challenges to traditional CFD methods. The DSMC method encounters excessive computational cost in the near-continuum regime and makes the simulation of the whole expansion process unacceptable. The UGKWP method is perfectly suitable for this case and yields a reliable multiscale solution with a reasonable computational cost.

The mesh adopted in this case is shown in Fig. 23. The physical mesh of the entire calculation domain has 83,776 cells, and the maximum number of particles in each cell is 200. Simulation results by the UGKWP method are compared with those of experiments and the DSMC-NS method [33]. In this section, the ambient pressure outside the nozzle is $P_\infty = 0.01$ Pa, and the ambient temperature is $T_\infty = 300$ K; At the inlet of the nozzle, the stagnation temperature is $T_s = 710$ K, and the stagnation pressure is $P_s = 4866.18$ Pa; The isothermal wall boundary condition is used for the nozzle wall with a temperature of $T_w = 500$ K.

To validate the accuracy of the simulation, the Pitot pressure and temperature along the central axis of the nozzle are shown in Fig. 24. A comparison is made among the solutions of UGKWP, experimental data, and the DSMC-NS method [33]. Reasonable agreements have been observed. A temperature jump at the nozzle throat is captured by

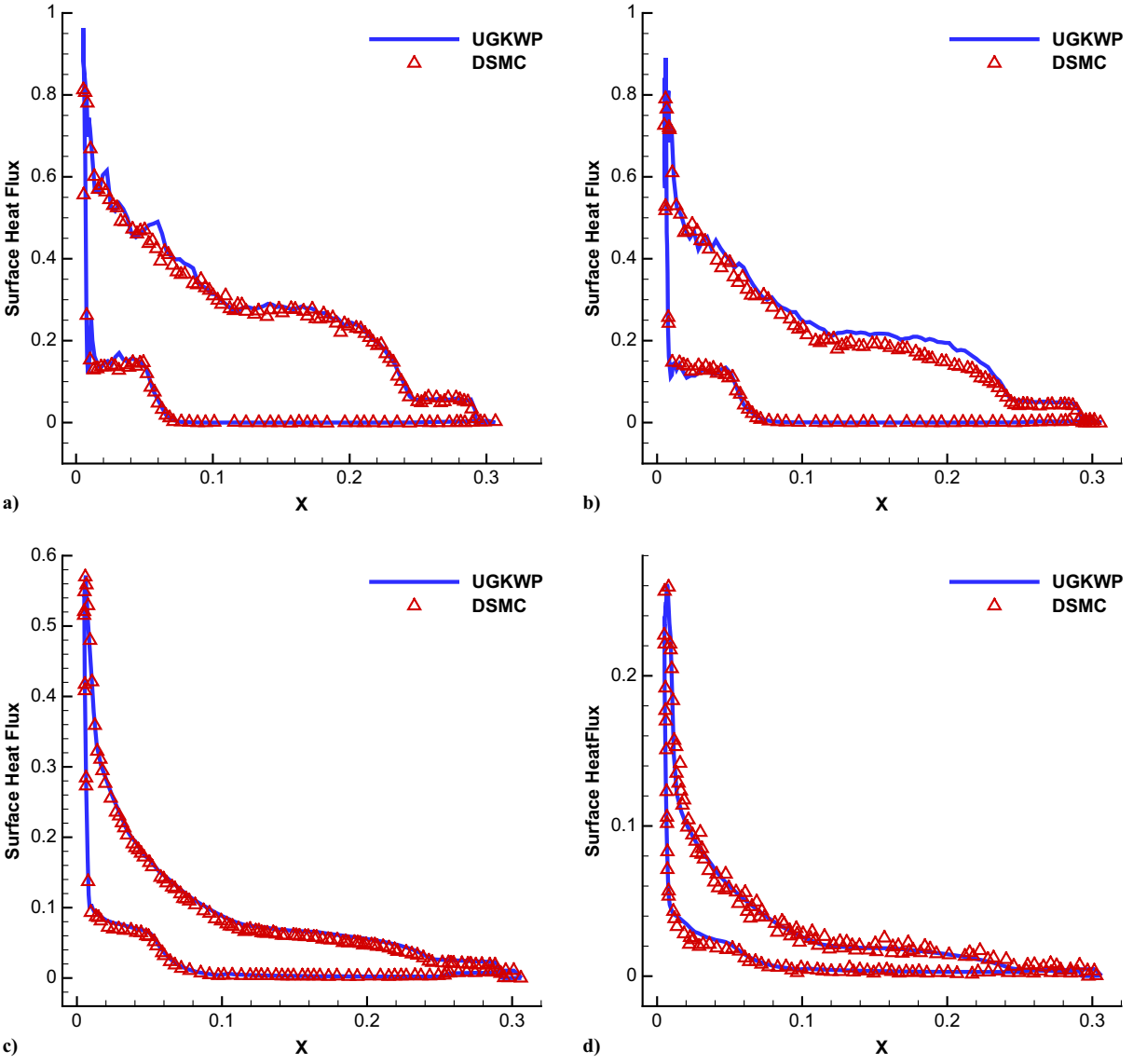

Fig. 21 Heat flux coefficients on the axial surface of X38-like vehicle at $Ma_\infty = 8.0$ with AoA $= 20^\circ$ by the UGKWP method. a) $Kn_\infty = 2.75$, b) $Kn_\infty = 0.275$, c) $Kn_\infty = 0.0275$, and d) $Kn_\infty = 0.00275$.

UGKWP, while the DSMC-NS method is unable to get it due to the loss of accuracy.

Figure 25 shows the temperature, x-component velocity distribution, and streamlines on the symmetry plane of the computational domain. In Fig. 25a, the temperature field shows that due to the influence of high-temperature gas at the inlet and the contraction effect at the nozzle throat, the inlet section temperature is significantly higher than in other regions, reaching up to a maximum value of 1100 K. The temperature near the solid wall of the nozzle is affected by the isothermal wall condition and is around 500 K. In the expansion section of the nozzle, the expansion effect causes the temperature to drop rapidly, reaching below 50 K far from the exit plane. The backflow region is less affected, with a temperature of around 300 K. In Fig. 25b, a sharp increase in velocity can be observed in the exhaust expansion section, and the velocity continues to rise rapidly after leaving the exit plane. In the backflow region, the velocity is generally below 50 m/s, indicating that the backflow is not intense. Streamlines in Fig. 25c demonstrate the vortex structure within the inlet section, as well as the expansion process after leaving the exit plane.

Figure 26 shows the unsteady process of nozzle plume expansion. The contours and corresponding line plots show the temperature distribution and the gradient-length-dependent local Knudsen number Kn_{GII} along the central axis at different simulation times. As shown in Fig. 26, Kn_{GII} exhibits a variation across seven orders of magnitude., indicating the existence of multiscale flow throughout the entire transport process.

Table 9 presents the computational cost of the UGKWP method in the current study. Simulation is taken on the SUGON computation platform, and the CPU model used is 7285H 32C 2.5 GHz.

D. Side-Jet Impingement on Hypersonic Flow

The complex interaction between the jet flow and shock waves generates unique flow structures. In this section, we focus on the flow structure of the interactions between jet flow and hypersonic flow simulated by the UGKWP method. Referring to the configuration of previous studies [34,35], a two-dimensional mesh is generated as shown in Fig. 27. Positioned at $x = 0.2$ m along the surface, the side jet nozzle has a diameter of 1 mm. The simulation employs a total of 13,980 cells, with the reference number of particles per cell in the UGKWP method set as $N_r = 200$.

The simulation parameters follow the setup in Karpuzcu's work [35] and are presented in Table 10.

Figure 28 illustrates the streamline, Mach number, temperature, and local Knudsen number distribution Kn_{GII}. Two upstream recirculation

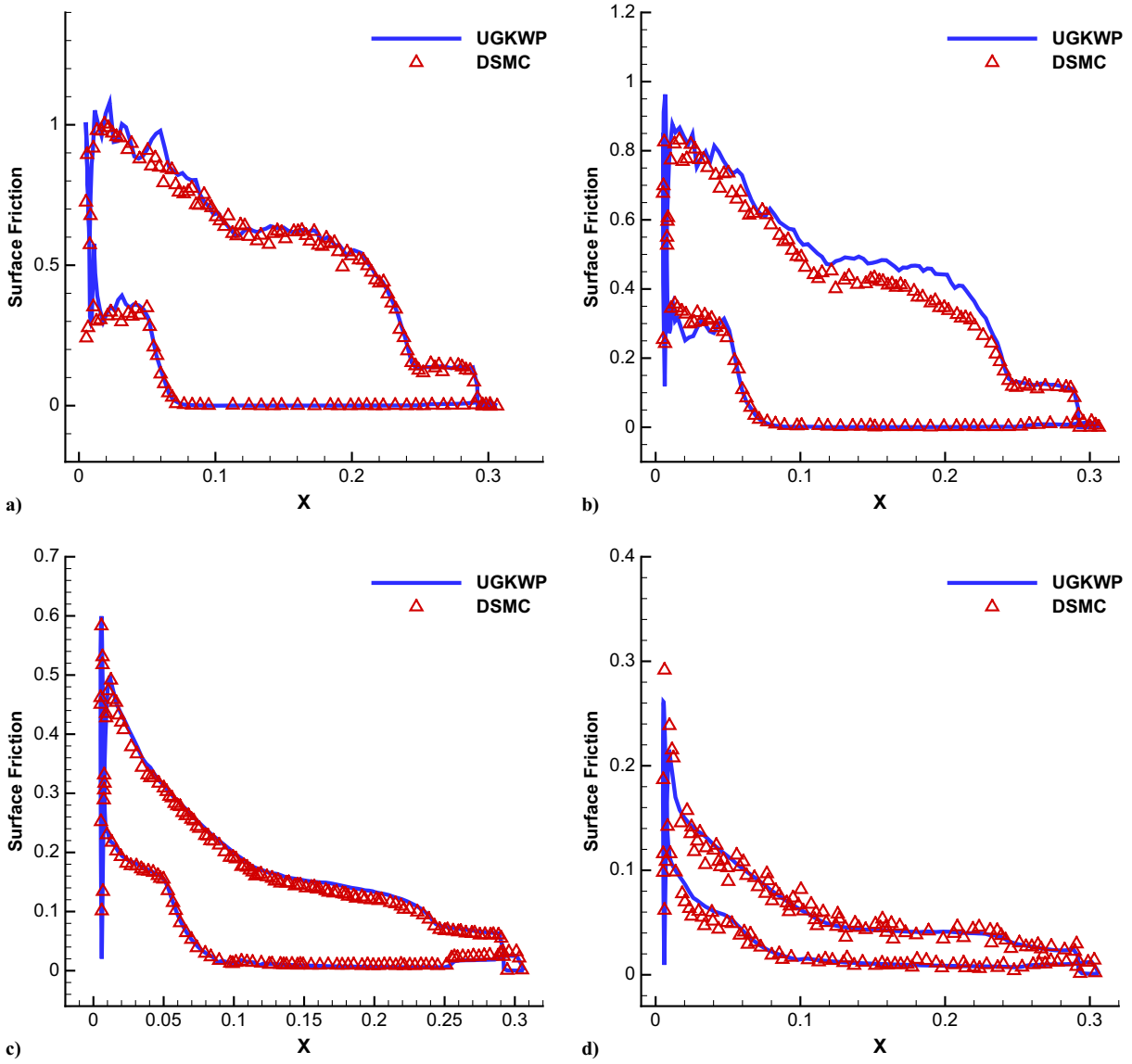

Fig. 22 Shear stress coefficients on the axial surface of X38-like vehicle at $Ma_\infty = 8.0$ with AoA $= 20°$ by the UGKWP method. a) $Kn_\infty = 2.75$, b) $Kn_\infty = 0.275$, c) $Kn_\infty = 0.0275$, and d) $Kn_\infty = 0.00275$.

zones and one downstream recirculation zone can be identified from the streamline plot. The expansion of the jet flow is restricted to a small area by a strong leading-edge shock, as the streamline from the nozzle changes the direction sharply. The gradient-length-dependent local Knudsen number distribution shows regions with shock and strong shear layers and their interaction.

A schematic diagram (see Fig. 29) is drawn on a continuous contour of Kn_{GII} to further describe the complex flow structure. Due to the presence of the jet, a separation shock forms and causes a strong separation layer, together with two recirculation zones. The jet expansion interacts with the separation shock, thus creating a strong bow shock. The hypersonic flow forces jet flow to reattach on the solid surface, creating the downstream recirculation zone.

A detailed comparison of flow structures is conducted. Specifically, the penetration height of the side jet, the length of primary upstream separation, secondary upstream separation, and downstream reattachment zones, and the angle between the bow shock, separation shear layer, and the solid surface, respectively, are compared as characteristic features. All flow structures are illustrated in Fig. 29. Tables 11 and 12 show the comparison of different flow characteristic parameters among the literature data, DSMC solution [35], and UGKWP simulation. The errors of the UGKWP method for each parameter are close to those of the DSMC method, and the overall errors compared to the literature data are less than 10%.

Table 13 presents the computational cost using the UGKWP method. Simulation is taken on the SUGON computation platform

Table 8 Computational cost for simulations of hypersonic flow around an X38-like vehicle at $Ma_\infty = 8.0$ by the UGKWP method

Kn_∞	AoA, °	Computation steps	Wall clock time, h	Cores	Estimated memory, GiB
0.00275	20	40,000 + 14,000[a]	7.33	640	9.28
0.0275	20	40,000 + 14,000[a]	13.6	640	57.7
0.275	20	40,000 + 12,000[a]	8.15	640	29.5
2.75	20	40,000 + 12,000[a]	11.1	640	35.4
0.00275	0	40,000 + 10,000[a]	6.58	640	9.61
0.0275	0	40,000 + 14,000[a]	15.1	640	60.0
0.275	0	40,000 + 12,000[a]	8.22	640	29.8
2.75	0	40,000 + 12,000[a]	12.3	640	36.6

The physical domain consists of 246,558 cells for cases at $Kn_\infty = 0.00275$ and 560,593 cells for others, and the reference number of particles per cell in the UGKWP method is set as $N_r = 150$.

[a]Steps of averaging process in UGKWP simulation.

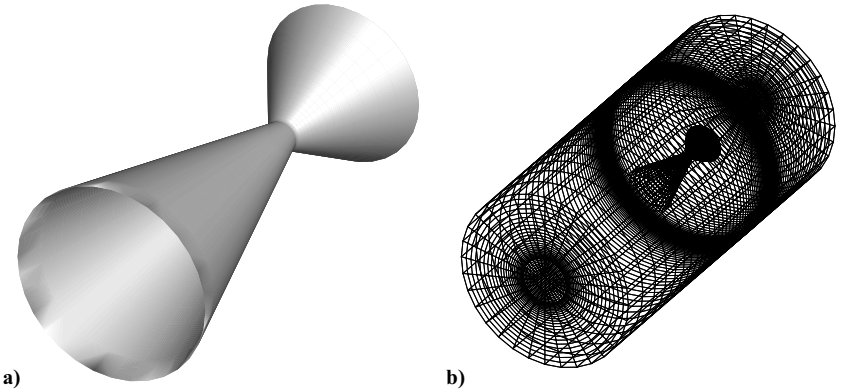

a) b)

Fig. 23 Geometry shape and the physical domain of nozzle plume expanding into a vacuum. a) Geometry shape, and b) physical mesh with 83,776 cells.

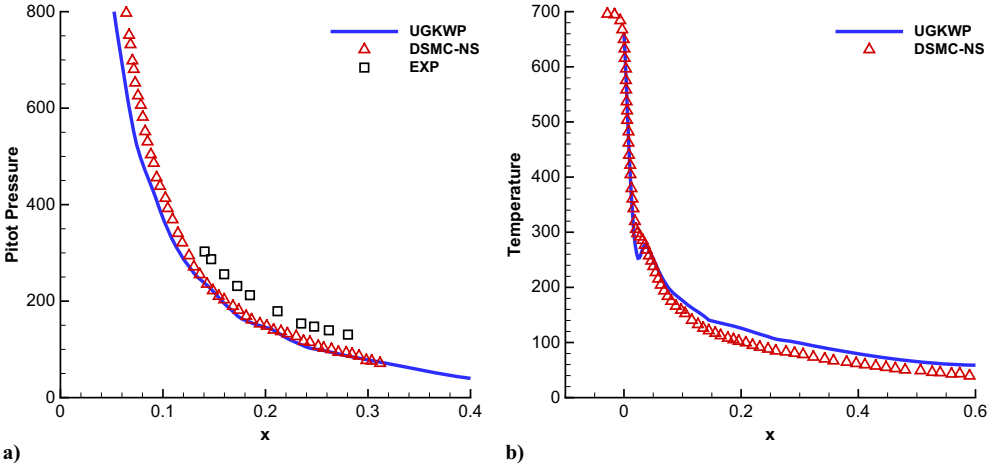

a) b)

Fig. 24 Pitot pressure and temperature profiles along the axis of the nozzle by the UGKWP method. a) Pitot pressure, and b) temperature.

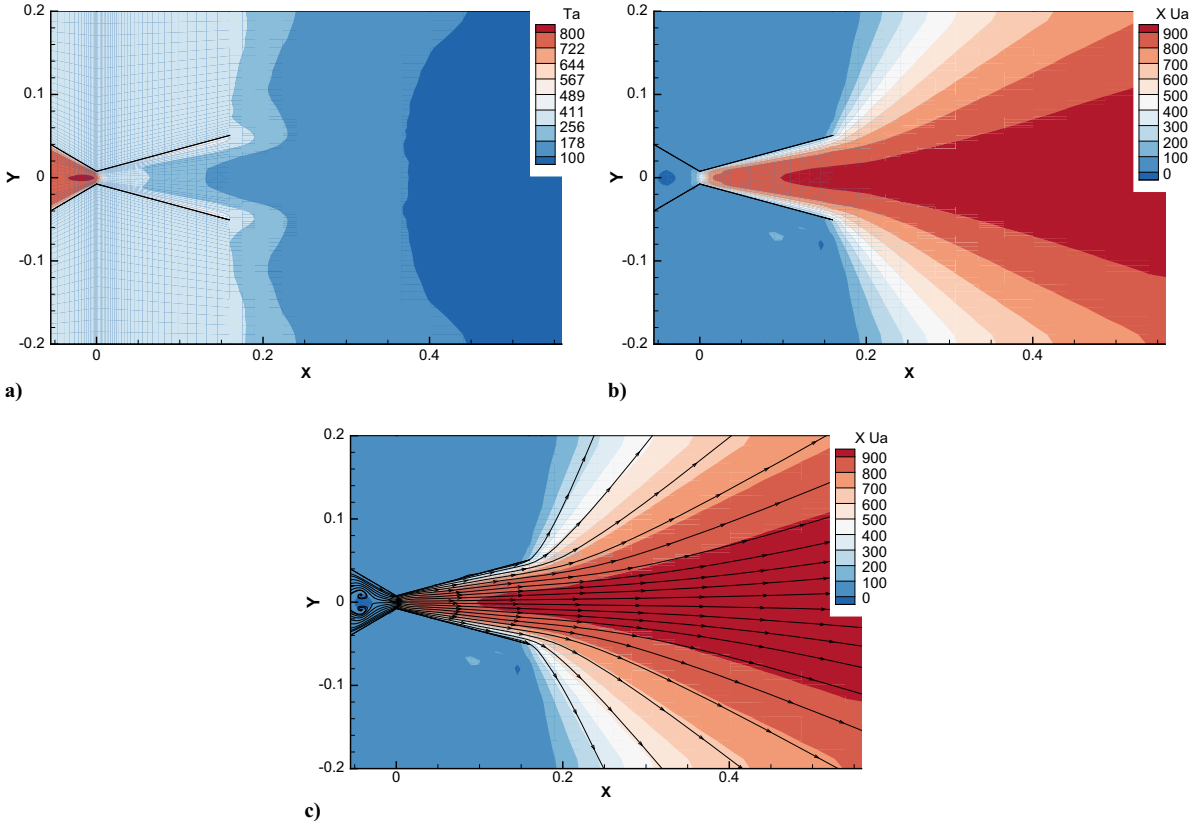

a) b)

c)

Fig. 25 Nozzle plume expanding to vacuum by the UGKWP method. a) Temperature, b) *x*-component velocity contours, and c) streamlines.

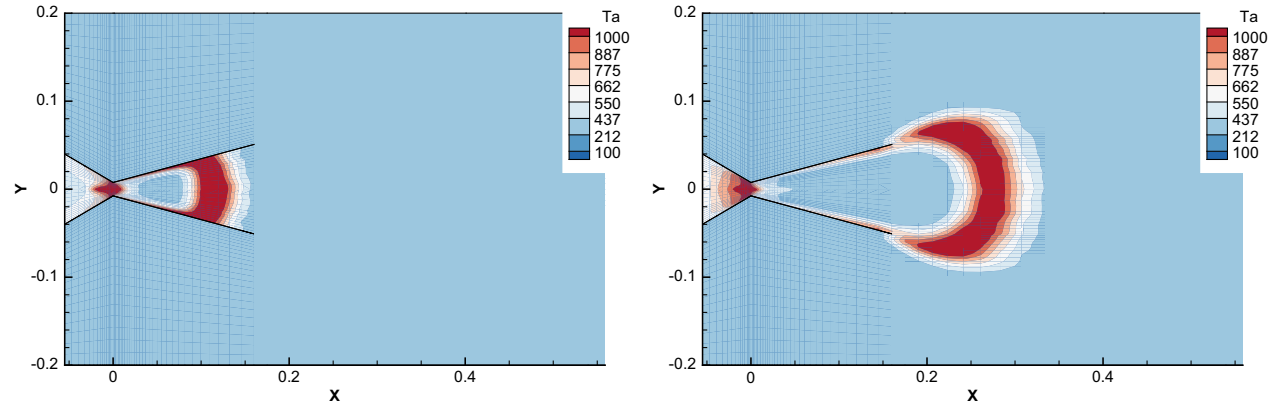

a) t=0.000100025 temperature contour

b) t=0.000199976 temperature contour

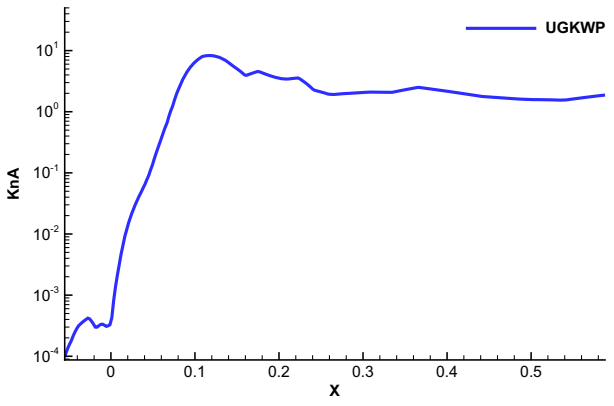

c) t=0.000100025 Kn_{GII} distribution line

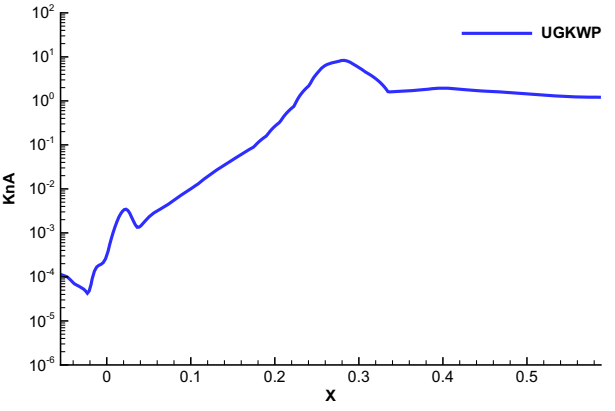

d) t=0.000199976 Kn_{GII} distribution line

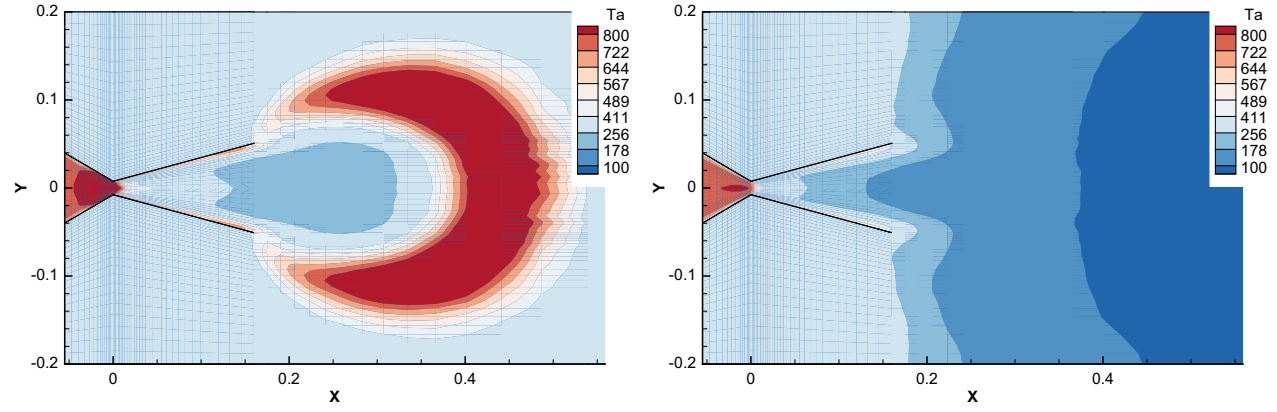

e) t=0.000299987 temperature contour

f) t=0.00295003 temperature contour

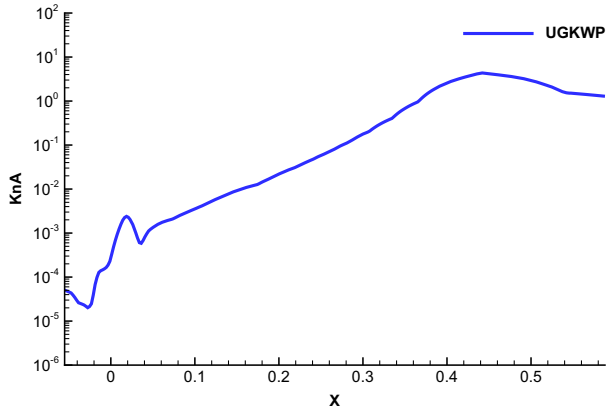

g) t=0.000299987 Kn_{GII} distribution line

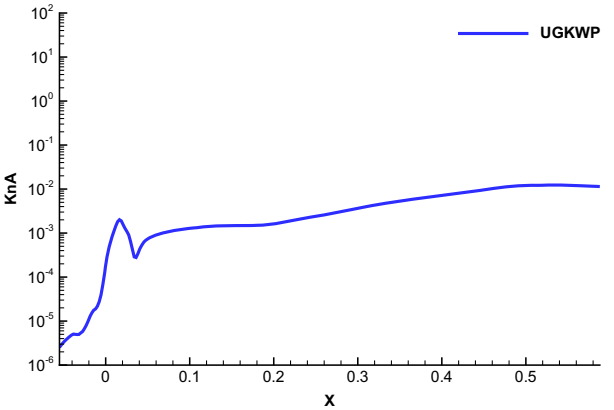

h) t=0.00295003 Kn_{GII} distribution line

Fig. 26 Distribution of gradient-length local Knudsen number Kn_{GII} and temperature on the symmetry plane of nozzle by the UGKWP method.

Table 9 Computational cost for the simulation of nozzle plume expansion into vacuum by the UGKWP method

Computation steps	Wall clock time, h	Cores	Estimated memory, GiB
6,000 + 15,000[a]	2.94	128	0.92

The physical domain consists of 83,776 cells, and the reference number of particles per cell in the UGKWP method is set as $N_r = 200$.
[a]Steps of time-averaging process in the UGKWP simulation.

Table 10 Freestream flow and jet flow parameters

Flow region	Freestream	Side jet
Molecule number density, m^{-3}	0.5×10^{22}	8.25×10^{23}
Mach number	12.0	1.0
Temperature, K	50.0	250.0
Pressure, Pa	3.45	2847.4
Knudsen number	0.15	0.0013

The gas used for the simulation is nitrogen.

with the CPU model 7285H 32C 2.5 GHz. A DSMC simulation of the same case by DS2V [36] employed 0.80 GiB of memory and cost 1.347 h. Therefore, for multiscale flow problems with strong non-equilibrium effects, the UGKWP method is more efficient.

E. Interaction of Hypersonic Flow with an Annular Jet over a Three-Dimensional Cone

In this section, hypersonic flow passing over a three-dimensional cone interacting with a ring of transverse jets is simulated. The

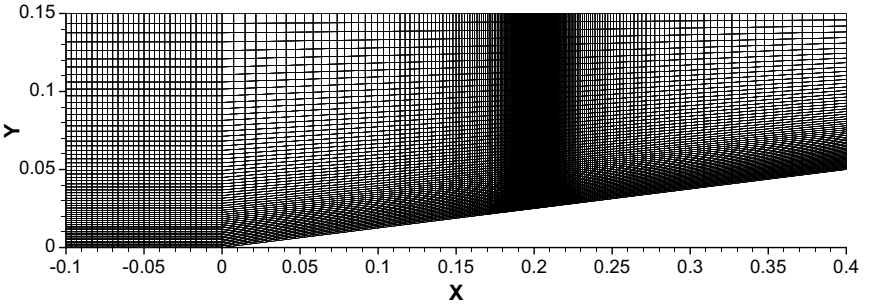

Fig. 27 Physical domain of the side-jet interaction with hypersonic flow.

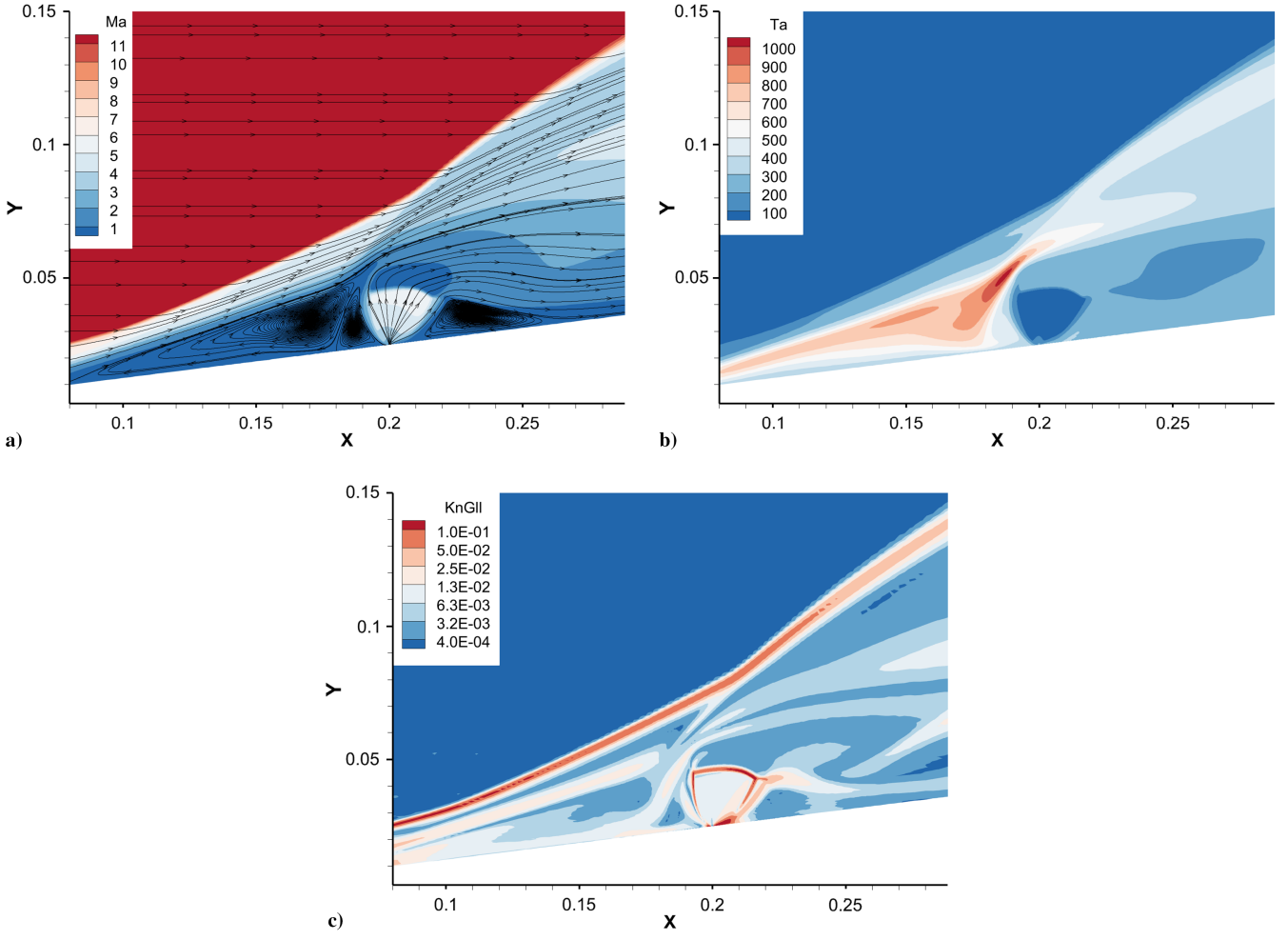

Fig. 28 Flow structures of hypersonic freestream flow at $Ma_\infty = 12.0$ and $Kn_\infty = 0.15$ interacting with a side-jet at $Ma_\infty = 1.0$ and $Kn_\infty = 0.0013$ by the UGKWP method. a) Mach number with streamlines, b) temperature, and c) local Knudsen number contours.

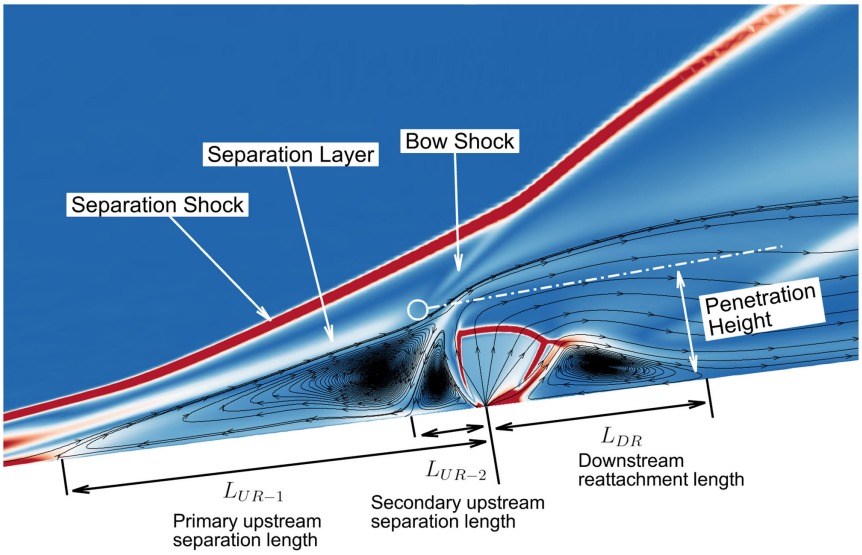

Fig. 29 A schematic diagram depicting several main flow structures of the hypersonic flow-jet interaction.

Table 11 Comparison of the separation and reattachment lengths in hypersonic flow-jet interaction by the UGKWP method with literature data

Source	h/r_b	$\theta_{BS}/^\circ$	$\theta_{SL}/^\circ$
Literature	0.523	13	33
DSMC	0.5	11	33
UGKWP	0.564	13.6	33.6
Error (with literature), %	7.84	4.61	1.82

Table 12 Comparison of the separation and reattachment lengths in hypersonic flow-jet interaction by the UGKWP method with DSMC data

Source	L_{UR-1}/h	L_{UR-2}/h	L_{DR}/h
DSMC	3.32	0.55	1.81
UGKWP	3.26	0.658	1.71
Error (with DSMC), %	−1.80	−19.63	5.52

Table 13 Computational cost for the simulation of side-jet interaction with hypersonic flow by the UGKWP method

Computation steps	Wall clock time, h	Cores	Estimated memory, GiB
10,000 + 20,000[a]	0.53	128	0.189

The physical domain consists of 13,980 cells, and the reference number of particles per cell in the UGKWP method is set as $N_r = 200$.
[a]Steps of time-averaging process in the UGKWP simulation.

geometric model used is a 7° cone, with the cone's base diameter of 0.1 m and its height of 0.4 m. An annular jet with a width of 1 millimeter is positioned at a height of 0.2 m. The UGKWP method is used in the simulation. The mesh with 612,500 cells around the cone is shown in Fig. 30. The computation is performed on a symmetric half-cone domain, with a maximum particle capacity of 200 per cell.

The simulation parameters follow the setup in Karpuzcu's work [35], as presented in Table 14.

The surface normalized pressure p_n and heat flux coefficient C_h are calculated and shown in Fig. 31 together with a comparison with the DSMC data [35]. Good agreements have been observed. The normalization is taken below:

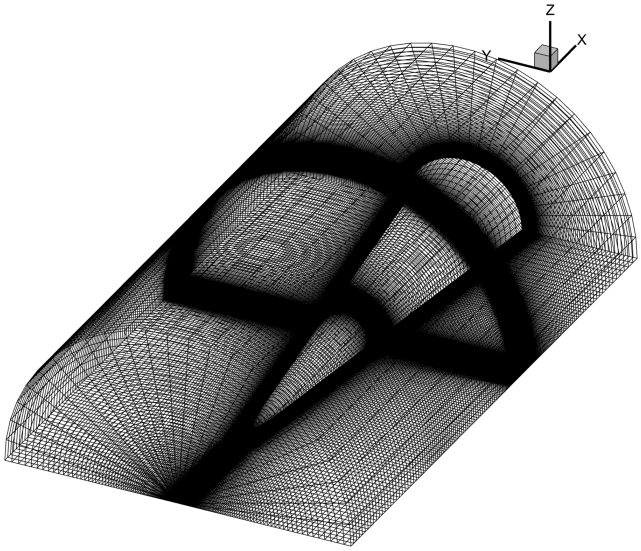

Fig. 30 Three-dimensional mesh over a cone for the simulation of the interaction between hypersonic flow and annular jet.

$$p_n = \frac{p_s}{p_\infty}, \qquad C_h = \frac{h_s}{(1/2)\rho_\infty C_\infty^3} \tag{19}$$

where $C_\infty = \sqrt{2RT_\infty}$, and T_∞ and ρ_∞ are temperature and density of freestream flow.

Figure 32 illustrates the streamline, Mach number, temperature, and local Knudsen number distribution Kn_{Gll}, all of which demonstrate a flow structure similar to the two-dimensional case. The recirculation zones and expansion area of the jet are much reduced

Table 14 Freestream flow and jet flow parameters

Flow region	Freestream	Side jet
Molecule number density, m^{-3}	1.0×10^{22}	1.65×10^{23}
Mach number	6.0	1.0
Temperature, K	50.0	250.0
Pressure, Pa	6.9	571.2
Knudsen number	0.07	0.0067

The gas used for the simulation is nitrogen.

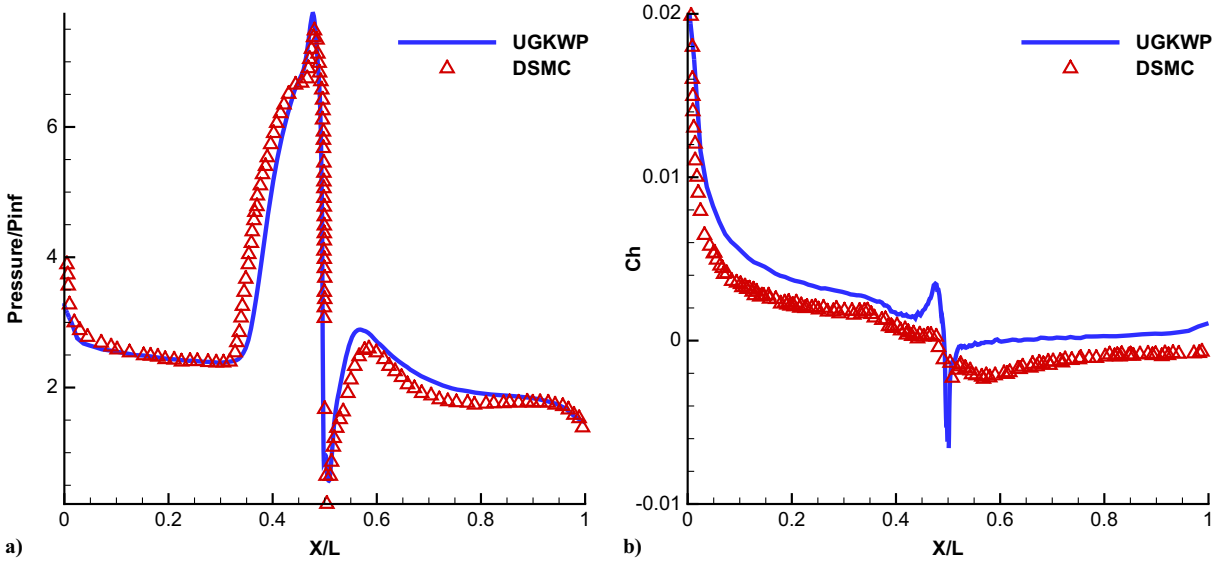

Fig. 31 Surface quantities of the three-dimensional cone by the UGKWP method. a) Surface normalized pressure, and b) surface heat flux coefficient.

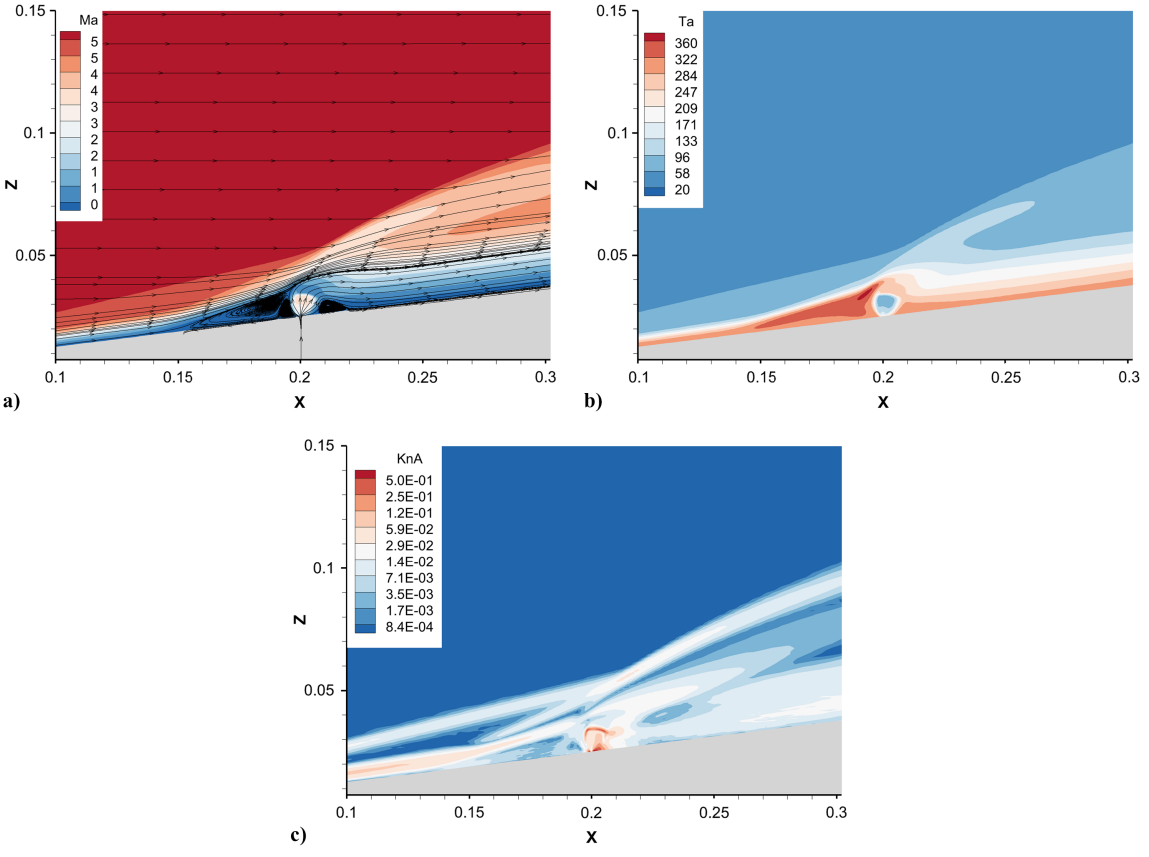

Fig. 32 Flow structures of Hypersonic freestream flow at $Ma_\infty = 6.0$ and $Kn_\infty = 0.07$ interacting with an annular jet at $Ma_\infty = 1.0$ and $Kn_\infty = 0.0067$ by the UGKWP method. a) Mach number with streamlines, b) temperature, and c) local Knudsen number contours.

Table 15 Computational cost for the simulation of hypersonic flow over a three-dimensional cone with an annular jet by the UGKWP method

Computation steps	Wall clock time, h	Cores	Estimated memory, GiB
28,000 + 7,000[a]	4.73	640	8.29

The physical domain consists of 612,500 cells, and the reference number of particles per cell in the UGKWP method is set as $N_r = 200$.
[a]Steps of time-averaging process in the UGKWP simulation.

due to the less intensified jet flow, the three-dimensional effect, and the low Mach number of the freestream flow.

Table 15 presents the computational cost in the simulation, which is taken on the SUGON computation platform with a CPU model of 7285H 32C 2.5 GHz.

IV. Conclusions

In this study, we employ the UGKWP method to examine several nonequilibrium flow issues. The adaptive wave-particle decomposition

enables the UGKWP method to efficiently capture multiscale effects in all flow regimes. The aerodynamic and aerothermodynamic characteristics of supersonic and hypersonic external flows over a sphere and an X38-like space vehicle agree well with experimental and DSMC data. The UGKWP method is able to capture nonequilibrium transport in all flow regimes and is exemplified in the simulation of nozzle plume expansion into a background vacuum, where solutions ranging from the continuum Navier–Stokes to the free molecular flow are accurately obtained. Complex flow structures resulting from the interaction of hypersonic flow with side-jets are accurately reproduced in the UGKWP simulation. For 3D simulations involving complex geometries, like the X38 vehicle with 560,593 cells in the computational domain, the UGKWP method consumes only 60 GiB of memory and takes less than 15 h to get the converged solutions, which is affordable for personal workstations. In conclusion, all the test cases in this study demonstrate the significant potential of the UGKWP method for engineering applications involving nonequilibrium multiscale transport. In the future work, more acceleration techniques will further enhance the application of the UGKWP method in the aerospace industry.

Acknowledgments

This work was supported by the National Key R&D Program of China (2022YFA1004500), the National Natural Science Foundation of China (Grant Nos. 12172316 and 92371107), and the Hong Kong Research Grant Council (16208021 and 16301222).

References

[1] Broadwell, J. E., "Study of Rarefied Shear Flow by the Discrete Velocity Method," *Journal of Fluid Mechanics*, Vol. 19, No. 3, 1964, pp. 401–414. https://doi.org/10.1017/S0022112064000817

[2] Zhihui, L., Xinyu, J., Junlin, W., and Aoping, P., "Gas-Kinetic Unified Algorithm for Boltzmann Model Equation in Rotational Nonequilibrium and Its Application to the Whole Range Flow Regimes," *Chinese Journal of Theoretical and Applied Mechanics*, Vol. 46, No. 3, 2014, pp. 336–351. https://doi.org/10.6052/0459-1879-13-246

[3] Zhang, R., Liu, S., Chen, J., Zhong, C., and Zhuo, C., "A Conservative Implicit Scheme for Three-Dimensional Steady Flows of Diatomic Gases in All Flow Regimes Using Unstructured Meshes in the Physical and Velocity Spaces," arXiv preprint arXiv:2303.10846, 2023. https://doi.org/10.48550/arXiv.2303.10846

[4] Jiang, D., "Study of the Gas Kinetic Scheme Based on the Analytic Solution of Model Equations," Ph.D. Thesis, China Aerodynamics Research and Development Center, Mianyang, PRC, May 2016.

[5] Macrossan, M. N., "Scaling Parameters in Rarefied Flow: Breakdown of the Navier-Stokes Equations," Univ. of Queensland Rept. 2006/03, 2006.

[6] Padilla, J., and Boyd, I., "Assessment of Rarefied Hypersonic Aerodynamics Modeling and Windtunnel Data," *9th AIAA/ASME Joint Thermophysics and Heat Transfer Conference*, AIAA Paper 2006-3390, 2006. https://doi.org/10.2514/6.2006-3390

[7] Loth, E., "Compressibility and Rarefaction Effects on Drag of a Spherical Particle," *AIAA Journal*, Vol. 46, No. 9, 2008, pp. 2219–2228. https://doi.org/10.2514/1.28943

[8] Loth, E., Tyler Daspit, J., Jeong, M., Nagata, T., and Nonomura, T., "Supersonic and Hypersonic Drag Coefficients for a Sphere," *AIAA Journal*, Vol. 59, No. 8, 2021, pp. 3261–3274. https://doi.org/10.2514/1.J060153

[9] Bird, G., "Approach to Translational Equilibrium in a Rigid Sphere Gas," *Physics of Fluids*, Vol. 6, 1963, pp. 1518–1519. https://doi.org/10.1063/1.1710976

[10] Rault, D. F., "Aerodynamics of the Shuttle Orbiter at High Altitudes," *Journal of Spacecraft and Rockets*, Vol. 31, No. 6, 1994, pp. 944–952. https://doi.org/10.2514/3.26542

[11] LeBeau, G., and Lumpkin, F., III, "Application Highlights of the DSMC Analysis Code (DAC) Software for Simulating Rarefied Flows," *Computer Methods in Applied Mechanics and Engineering*, Vol. 191, Nos. 6–7, 2001, pp. 595–609. https://doi.org/10.1016/S0045-7825(01)00304-8

[12] Justiz, C. R., Sega, R. M., Dalton, C., and Ignatiev, A., "DSMC- and BGK-Based Calculations for Return Flux Contamination of an Outgassing Spacecraft," *Journal of Thermophysics and Heat Transfer*, Vol. 8, No. 4, 1994, pp. 802–803. https://doi.org/10.2514/3.617

[13] Gimelshein, S., Gimelsheint, N., Levin, D., Ivmov, M., and Markelov, G., "Modeling of Rarefied Hypersonic Flows over Spacecraft in Martian Atmosphere Using the DSMC Method," *8th AIAA/ASME Joint Thermophysics and Heat Transfer Conference 2002*, AIAA Paper 2002-2759, 2002. https://doi.org/10.2514/6.2002-2759

[14] Zhang, W.-P., Han, B., and Zhang, C.-Y., "Spacecraft Aerodynamics and Trajectory Simulation During Aerobraking," *Applied Mathematics and Mechanics*, Vol. 31, No. 9, 2010, pp. 1063–1072. https://doi.org/10.1007/s10483-010-1342-x

[15] Ivanov, M., Vashchenkov, P., Markelov, G., Kashkovsky, A., and Krylov, A., "DSMC Study of the Near-Continuum Flow Near the Nose Part of the Spacecraft"Progress-M," *37th AIAA Thermophysics Conference*, AIAA Paper 2004-2688, 2004. https://doi.org/10.2514/6.2004-2688

[16] Ivanovich, K. Y., Myint, Z. Y. M., and Yurievich, K. A., "Aerodynamic Investigation for Prospective Aerospace Vehicle in the Transitional Regime," *International Journal of Aeronautical and Space Sciences*, Vol. 14, No. 3, 2013, pp. 215–221. https://doi.org/10.5139/IJASS.2013.14.3.215

[17] Titarev, V. A., Frolova, A. A., Rykov, V., Vashchenkov, P., Shevyrin, A., and Bondar, Y. A., "Comparison of the Shakhov Kinetic Equation and DSMC Method as Applied to Space Vehicle Aerothermodynamics," *Journal of Computational and Applied Mathematics*, Vol. 364, Jan. 2020, Paper 112354. https://doi.org/10.1016/j.cam.2019.112354

[18] Zuppardi, G., Savino, R., Russo, G., Spano'Cuomo, L., and Petrosino, E., "Aerodynamic Analysis of the Aerospaceplane HyPlane in Supersonic Rarefied Flow," *Acta Astronautica*, Vol. 123, Jan. 2016, pp. 229–238. https://doi.org/10.1016/j.actaastro.2016.03.025

[19] Zuppardi, G., Morsa, L., Sippel, M., and Schwanekamp, T., "Aero-Thermo-Dynamic Analysis of the SpaceLiner-7.1 Vehicle in High Altitude Flight," *AIP Conference Proceedings*, Vol. 1628, No. 1, 2014, pp. 1268–1276. https://doi.org/10.1063/1.4902737

[20] Moss, J., "DSMC Simulations of Ballute Aerothermodynamics Under Hypersonic Rarefied Conditions," *38th AIAA Thermophysics Conference*, AIAA Paper 2005-4949, 2005. https://doi.org/10.2514/6.2005-4949

[21] Li, J., Jiang, D., Geng, X., and Chen, J., "Kinetic Comparative Study on Aerodynamic Characteristics of Hypersonic Reentry Vehicle from Near-Continuous Flow to Free Molecular Flow," *Advances in Aerodynamics*, Vol. 3, Dec. 2021, pp. 1–10. https://doi.org/10.1186/s42774-021-00063-0

[22] Xu, K., *Direct Modeling for Computational Fluid Dynamics: Construction and Application of Unified Gas-Kinetic Schemes*, Vol. 4, World Scientific, Singapore, 2014. https://doi.org/10.1017/9781108877534

[23] Liu, C., Zhu, Y., and Xu, K., "Unified Gas-Kinetic Wave-Particle Methods I: Continuum and Rarefied Gas Flow," *Journal of Computational Physics*, Vol. 401, Jan. 2020, Paper 108977. https://doi.org/10.1016/j.jcp.2019.108977

[24] Zhu, Y., Liu, C., Zhong, C., and Xu, K., "Unified Gas-Kinetic Wave-Particle Methods. II. Multiscale Simulation on Unstructured Mesh," *Physics of Fluids*, Vol. 31, No. 6, 2019, Paper 067105. https://doi.org/10.1063/1.5097645

[25] Xu, K., "A Gas-Kinetic BGK Scheme for the Navier–Stokes Equations and Its Connection with Artificial Dissipation and Godunov Method," *Journal of Computational Physics*, Vol. 171, No. 1, 2001, pp. 289–335. https://doi.org/10.1006/jcph.2001.6790

[26] Wei, Y., Zhu, Y., and Xu, K., "Unified Gas-Kinetic Wave-Particle Methods VII: Diatomic Gas with Rotational and Vibrational Nonequilibrium," *Journal of Computational Physics*, Vol. 497, Jan. 2024, Paper 112610. https://doi.org/10.1016/j.jcp.2023.112610

[27] Li, W., Liu, C., Zhu, Y., Zhang, J., and Xu, K., "Unified Gas-Kinetic Wave-Particle Methods III: Multiscale Photon Transport," *Journal of Computational Physics*, Vol. 408, May 2020, Paper 109280. https://doi.org/10.1016/j.jcp.2020.109280

[28] Liu, C., and Xu, K., "Unified Gas-Kinetic Wave-Particle Methods IV: Multi-Species Gas Mixture and Plasma Transport," *Advances in Aerodynamics*, Vol. 3, No. 1, 2021, pp. 1–31. https://doi.org/10.1186/s42774-021-00062-1

[29] Yang, X., Wei, Y., Shyy, W., and Xu, K., "Unified Gas-Kinetic Wave-Particle Method for Three-Dimensional Simulation of Gas-Particle Fluidized Bed," *Chemical Engineering Journal*, Vol. 453, Feb. 2023, Paper 139541. https://doi.org/10.1016/j.cej.2022.139541

[30] Chen, Y., Zhu, Y., and Xu, K., "A Three-Dimensional Unified Gas-Kinetic Wave-Particle Solver for Flow Computation in All Regimes," *Physics of Fluids*, Vol. 32, No. 9, 2020, Paper 096108. https://doi.org/10.1063/5.0021199

[31] Wei, Y., Cao, J., Ji, X., and Xu, K., "Adaptive Wave-Particle Decomposition in UGKWP Method for High-Speed Flow Simulations," 2023. https://doi.org/10.21203/rs.3.rs-2772346/v1

[32] Venkatakrishnan, V., "Convergence to Steady State Solutions of the Euler Equations on Unstructured Grids with Limiters," *Journal of Computational Physics*, Vol. 118, No. 1, 1995, pp. 120–130. https://doi.org/10.1006/jcph.1995.1084

[33] George, J., and Boyd, I., "Simulation of Nozzle Plume Flows Using a Combined CFD-DSMC Approach," *33rd Thermophysics Conference*, AIAA Paper 1999-3454, 1999. https://doi.org/10.2514/6.1999-3454

[34] Karpuzcu, I. T., Levin, D. A., Mamrol, D., Wagner, L. N., Noftz, M. E., Jewell, J. S., and Smith, S. T., "Jet Flow-Shockwave Interactions in a Hypersonic Flow Using Experimental and Kinetic Methods," *AIAA Scitech 2022 Forum*, AIAA Paper 2022-1577, 2022. https://doi.org/10.2514/6.2022-1577

[35] Karpuzcu, I. T., and Levin, D. A., "Study of Side-Jet Interactions over a Hypersonic Cone Flow Using Kinetic Methods," *AIAA Journal*, Vol. 61, No. 11, 2023, pp. 4741–4751. https://doi.org/10.2514/1.J063020

[36] Bird, G. A., *Molecular Gas Dynamics and the Direct Simulation of Gas Flows*, Oxford Univ. Press Inc., New York, 1994. https://doi.org/10.1093/oso/9780198561958.001.0001

S. Fu
Associate Editor